Biomaterials 284 (2022) 121473

Contents lists available at ScienceDirect

Biomaterials

journal homepage: www.elsevier.com/locate/biomaterials

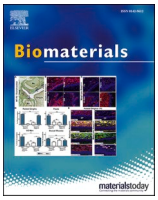

Hydrogels derived from decellularized liver tissue support the growth and differentiation of cholangiocyte organoids

Jorke Willemse [a], Gilles van Tienderen [a,1], Eline van Hengel [a,1], Ivo Schurink [a], Diana van der Ven [a], Yik Kan [a], Petra de Ruiter [a], Oskar Rosmark [d], Gunilla Westergren-Thorsson G [d], Kerstin Schneeberger [c], Bram van der Eerden [b], Henk Roest [a], Bart Spee [c], Luc van der Laan [a], Jeroen de Jonge [a], Monique Verstegen [a,*]

[a] Department of Surgery, Transplant Institute, Erasmus MC, University Medical Center Rotterdam, the Netherlands
[b] Department of Internal Medicine, Calcium and Bone Metabolism, Erasmus MC-University, Rotterdam, the Netherlands
[c] Department of Clinical Sciences of Companion Animals, Faculty of Veterinary Medicine, Utrecht University, Utrecht, the Netherlands
[d] Lung Biology, Department Experimental Medical Science, Lund University, Lund, Sweden

ARTICLE INFO

Keywords:
Human intrahepatic cholangiocyte organoids
Hepatobiliary tissue engineering and regenerative medicine
Whole organ perfusion-based liver decellularization
Liver extracellular matrix extracts
Extracellular matrix based hydrogel

ABSTRACT

Human cholangiocyte organoids are promising for regenerative medicine applications, such as repair of damaged bile ducts. However, organoids are typically cultured in mouse tumor-derived basement membrane extracts (BME), which is poorly defined, highly variable and limits the direct clinical applications of organoids in patients. Extracellular matrix (ECM)-derived hydrogels prepared from decellularized human or porcine livers are attractive alternative culture substrates. Here, the culture and expansion of human cholangiocyte organoids in liver ECM(LECM)-derived hydrogels is described. These hydrogels support proliferation of cholangiocyte organoids and maintain the cholangiocyte-like phenotype. The use of LECM hydrogels does not significantly alter the expression of selected genes or proteins, such as the cholangiocyte marker cytokeratin-7, and no species-specific effect is found between human or porcine LECM hydrogels. Proliferation rates of organoids cultured in LECM hydrogels are lower, but the differentiation capacity of the cholangiocyte organoids towards hepatocyte-like cells is not altered by the presence of tissue-specific ECM components. Moreover, human LECM extracts support the expansion of ICO in a dynamic culture set up without the need for laborious static culture of organoids in hydrogel domes. Liver ECM hydrogels can successfully replace tumor-derived BME and can potentially unlock the full clinical potential of human cholangiocyte organoids.

1. Introduction

Intrahepatic cholangiocyte organoids (ICO) are a valuable source of hepatobiliary cells for tissue engineering and regenerative medicine applications [1–4]. These organoids can be initiated from relatively small liver biopsies and give rise to large numbers of genetically stable cells [1,5,6]. Cholangiocyte organoids have shown to efficiently repair damaged bile ducts *ex vivo* [7,8] and can potentially be used to fully repopulate the biliary network of decellularized human livers [9]. ICO also have the ability to differentiate towards hepatocyte-like cells, making them a potential source of hepatocytes as well [1,5,10]. ICO are therefore relevant for preparing *in vitro* tissue engineered liver constructs that can be used for tissue engineering and regenerative medicine (TERM) applications, such as bridging therapies, auxiliary liver transplantation or complete replacement of hepatobiliary tissue [2,3,11].

However, these future clinical applications are currently limited by the use of mouse tumor-derived basement membrane extracts (BME) in which ICO are typically cultured. The commercially available extracts (e.g. Corning Matrigel or Cultrex BME) provide the cells with a bioactive micro-environment in which they can proliferate and self-organize into spherical structures [12,13]. BME is derived from the tumor extracellular matrix (ECM) produced by Englebreth-Holm-Swarm (EHS) mouse

* Corresponding author. Erasmus MC-University Medical Center, Department of Surgery, Dr. Molewaterplein 40, Room Na1005, 3015 GD, Rotterdam, the Netherlands.
E-mail address: m.verstegen@ermasmusmc.nl (M. Verstegen).
[1] Authors contributed equally.

https://doi.org/10.1016/j.biomaterials.2022.121473
Received 5 October 2021; Received in revised form 4 March 2022; Accepted 15 March 2022
Available online 24 March 2022

cells. These cells produce an abundance of basement membrane components, such as laminin-111, collagen type IV and entactin [12–16]. However, it should be mentioned that large batch-to-batch variations are known to exist [12]. The mouse tumor origin of the extracts and relative large variability are hampering production of clinical-grade extracts. Therefore, the ICO grown in BME cannot be used for clinical applications. In addition, the use of BME stimulates cell proliferation and maintains stem cell phenotypes [17,18]. This, combined with the facts that BME lacks tissue-specific (bio)chemical cues and/or ECM components, could impede cell differentiation.

The importance of liver-specific ECM components to support cell proliferation and differentiation *in vivo* is illustrated by the vital role the liver extracellular matrix (LECM) plays in embryonic development of hepatic tissue, maintaining organ homeostasis and regeneration after damage [19–21]. Moreover, alterations in the composition of LECM are linked to the development of diseases, such as fibrosis and/or cirrhosis [21,22]. The LECM is a highly complex and dynamic environment, which is challenging to mimic *in vitro* [23]. Synthetic hydrogels have shown to support organoid growth, but often do not approach the tissue's biochemical complexity [24–28]. In many cases, these 'bare' synthetic hydrogels are decorated with ECM extracts derived from the mouse tumor cells [28–30]. Alternatively, tissue-specific ECM components, derived from healthy decellularized livers, can be used to create tissue-specific liver-derived hydrogels [30,31]. Decellularized ECMs have been allowed for clinical applications [32,33], thus tissue-specific liver-derived hydrogels can be used to generate clinical-grade ICO. Similar approaches with tissue-specific ECM hydrogels have been studied for replacing BME for other types of organoids [34–38].

Liver ECM components can be sourced from decellularized human livers, but also from animal livers, such as porcine livers, because these ECM components are highly preserved between species [30]. However, human liver ECM (HLECM) is not completely similar to porcine liver ECM (PLECM), since anatomical differences between the liver exist. Hepatic lobules in porcine livers are separated by dense septa, which are not present in healthy human livers [39]. These septa can only be found in fibrotic human livers [20,39]. These septa are made of collagen and their presence could shift the relative distribution of the ECM in the ECM extracts. This ultimately could influence cellular behavior [40].

Hydrogels made from solubilized LECM are an alternative to BME, particularly as a tissue-specific and clinically applicable culture substrate for ICO expansion [33,41–43]. The use of these healthy LECM extracts could thus also unlock the full clinical potential of the ICO by providing them with a clinically relevant tissue-specific *in vitro* microenvironment. The aim of this study is to investigate whether hydrogels derived from healthy porcine LECM (PLECM) or human LECM (HLECM) can replace mouse tumor-derived BME for the culture and expansion of ICO. We hypothesize that these clinical and biological relevant culture substrates support (large-scale) expansion of the organoids.

2. Material and methods

2.1. Liver procurement

2.1.1. Porcine livers for decellularization

Porcine livers (N = 7) were obtained from healthy pigs (weight range: 30–40 kg). The animals were used for acute terminal medical research experiments (DEC 105-14-05). The use of liver tissue for decellularization purposes was allowed by the animal welfare committee of the Erasmus University Medical Center to comply with the 3R rule (replacement, reduction and refinement). The animals were heparinized (300 IU/kg body weight) before euthanasia. The liver was cannulated via the portal vein and hepatic artery. After procurement, the liver was flushed with cold 0.9% NaCl and stored at −20 °C.

2.1.2. Human research livers for decellularization

Human livers, deemed unsuitable for transplantation, were obtained after declination for liver transplantation by all transplant centers in the Eurotransplant (ET) zone. Informed consent for use of these livers for research purposes was given to transplant coordinators of the Dutch Transplant Foundation (NTS) by next of kin and was approved by the Erasmus MC medical ethics committee (MEC-2012-090). Human livers (N = 4) were retrieved by specialized organ retrieval teams according to the ET manual, chapter 5. The livers were stored in University of Wisconsin (UW, bridge to life) preservation fluid on melting ice and transported to the Erasmus University Medical Center. Organs were stored at −20 °C after the portal vein and hepatic artery were cannulated.

2.1.3. Human donor liver biopsies for organoid cultures

For the initiation of human intrahepatic cholangiocyte organoids (ICO), liver biopsies (0.5 cm^3–1$cm^{3)}$ from healthy donor livers (N = 39) were obtained during liver transplantation procedures at the Erasmus MC. The use of liver biopsies for research purposes was approved by the medical ethics committee of the Erasmus University Medical center (MEC-2014-060). The biopsies were stored in UW on melting ice. All liver biopsies were viable frozen in recovery freeze medium (Table S1) and stored in liquid nitrogen until used for ICO initiation.

2.1.4. Decellularization procedure

2.1.4.1. Porcine liver. Porcine livers were decellularized by perfusion with Triton-X-100 (4%, Tx100) as previously described [9]. In short, porcine livers were thawed and flushed with 20 L dH_2O. Subsequently, 10 L of 4% Tx100 + 1% NH_3 (Tx100 solution) was perfused continuously through the liver. Perfusion rates were pressure controlled and the upper limit for the hepatic artery was set at 120 mm Hg. Subsequently, 10 L Tx100 solution was reperfused for 120 min. In total, five 120 min cycles were used. Afterwards, the livers were continuously perfused with 50 L dH_2O before being stored at 4 °C for 10–14 days in 10 L dH_2O, which was replaced every other day. Finally, the livers were perfused with DNase solution 5 mg/L DNase type I (Sigma) in 0.9% NaCl + 100 mM $CaCl_2$ + 100 mM $MgCl_2$) for 120 min.

2.1.4.2. Human liver. Human livers (N = 4) were decellularized as previously described [9]. In short, the human livers were thawed and flushed with 50 L dH_2O. Subsequently, the livers were continuously perfused with Tx100 solution for 120 min. The livers were further decellularized by ten 120 min reperfusion cycles with 10 L Tx100 solution. Afterwards, the livers were flushed with 100 L dH_2O and stored in sealed containers with 10 L dH_2O for 10–14 days. The dH_2O was refreshed every other day. The final step consisted of an 8 h reperfusion cycle with DNase solution (10 mg/L DNase type I (Sigma) in 0.9% NaCl + 100 mM $CaCl_2$ + 100 mM $MgCl_2$).

2.1.5. Confirmation of decellularization

Two biopsies were taken per liver before and after decellularization procedures. One sample was fixed in 4% paraformaldehyde (PFA, Fresenius Kabi) and one sample was snap frozen and stored at −80 °C. PFA-fixed biopsies were embedded in paraffin, 4 μm sectioned were obtained and stained with Hematoxylin-Eosin (HE) or 4′,6-diamidino-2-phenylindole (DAPI, Vectashield, Vectorlabs). HE stained slides were imaged with a Zeiss Axioskop 20 microscope and captured with a Nikon DS-U1 camera. DAPI stained slides were analyzed using EVOS microscope (Thermofisher). The snap frozen biopsies were used for DNA quantification. Prior to DNA isolation the wet weight of the biopsies was measured. DNA was isolated using a QIAamp DNA Mini Kit (QIAGEN) kit according to manufacturer's protocol. DNA yield was measured using a NanoDrop spectrophotometer (Thermo Fisher Scientific). RNA for detection of porcine endogenous retrovirus (PERV) was isolated using the miRNeasy (Qiagen) kit according to manufacturers' protocol. RNA yield was measured using a Nanodrop 2000. RT-qPCR was performed using SYBR select master mix for SFX (Applied Biosystems) on a

StepOnePlus RT PCR system (Applied Biosystems). Primers used are listed in Table S7 [44].

2.1.6. Hydrogel preparation

PLECM and HLECM were prepared by removing the Glisson's capsule and cutting the ECM in smaller cuboidal fragments using surgical scissors (~0.1–0.5 cm^3). The ECM was frozen at −20 °C and freeze-dried using a lyophilizer (Zirbus Technology Sublimator 400) over a period of 72–96 h. Subsequently, the freeze-dried ECM was pulverized using a Retsch ZM200 knife mill with a <200 μm sieve.

PLECM and HLECM were digested at a concentration of 40 mg/ml in 10%(W/W) Pepsin (Sigma, 3,200-4,500U/mg) in 0.5 M Acetic Acid over a 72-h period at RT. Afterwards, the mixtures were cooled on melting ice for 30–60 min 10%(V/V) 10X PBS and 10%(V/V) ADV+ (Table S2) was added. pH was adjusted to 7.4–7.6 using 5 M NaOH. Final pH adjustments were made with 1 M NaOH or 1 M HCl until the color indicator of the ADV + switched from yellow to pink/orange. Small aliquots were taken to confirm the desired pH with an electronic pH meter (VWR symphony SB70P). After setting the pH, the digested LECM was diluted to 8 mg/ml. This is considered the 'stock concentration' of the pre-gel solution. The pre-gel solutions were spun down at 1811RCF (30 min, 4 °C) in order to remove undigested debris.

50 μl of each batch of pre-gel solution was plated in a 24-well plate and the plate was placed in a humidified CO_2 incubator at 37 °C for 30–45 min. Gelation of the droplets was confirmed by rotating the plate upside down. PLECM (N = 7) or HLECM (N = 6) pre-gel solutions were pooled together after successful inversion tests. The pre-gel solutions were aliquoted and used directly or stored at −20 °C.

2.2. Hydrogel characterization

2.2.1. Biochemical analysis

The degree of protein digestion was determined using a Pierce BCA assay kit (ThermoFisher) according to manufacturer's protocol. The absorbance was measured at 562 nm using an infinite M nano plate reader (TECAN). The total collagen content was measured using a total collagen kit (QuickZyme biosciences) according to manufacturer's protocol. Absorbance was measured at 570 nm using an infinite M nano plate reader (TECAN). A Glycosaminoglycan (GAG) assay kit (Biocolor) was used to measure GAG content according to manufacturer's protocol. The overall protein concentration of the samples was used to normalize the results. Samples were digested at 65 °C with Papain (10 mg/ml, Sigma) for 8 h. Absorbance was measured at 680 nm using a Model 680 XR Microplate Reader (Bio-Rad).

Human growth factors were quantified using a Quantibody Human Growth Factor Array Q1 (RayBioTech) according to manufacturers' protocol. In short, samples were weighed, placed in RIPA buffer and sonicated. The protein concentration of the lysate was measured using the BCA assay and protein input in growth factor array was normalized to 0.75 mg/ml. The microarray was imaged using a Typhoon 5 laser scanner (Cytiva). Analysis was performed using ImageJ. Growth factors with unreliable standard curves were omitted.

2.2.2. Mechanical properties

A MCR 301 Rheometer (Anton-Paar) using parallel plates (Diameter: 25 mm, 0°) was used in oscillatory mode to determine the storage (G') and loss (G") modulus. Cooled pre-gel samples (250 μl) were pipetted on the bottom plate, which was cooled to 4 °C. The test geometry was lowered to a gap height of 1 mm and excess hydrogel was discarded. The temperature was rapidly increased to 37 °C. Frequency (ω: 0.01–10 Hz, Slope: 10 pt./decimal) and strain sweeps (ϒ:0.01–10%, Slope:10 pt./decimal) were performed in order to determine the linear viscoelastic region. Every 10s a measurement was made and based on the results the linear viscoelastic region was determined. Subsequent time sweeps were performed with the following settings: ϒ: 0.5%, ω: 1 Hz. Time sweeps were performed with 1 measurement every 6s (150 measurements in total).

The effective Young's modulus was measured using a Piuma Nanoindenter (Optics11 Life). 50 μl of cold pre-gel droplets were pipetted into 35 mm petri dished and allowed to solidify inside a humidified CO_2 incubator at 37 °C for 24 h. The Piuma system was calibrated according to the manufacturer's protocol. The probe used had a stiffness of 0.062 N/m and a tip radius of 27 μm. Measurements were performed submerged in PBS. The indentation profile was default, except for the indentation depth (set to 15,000 nm) and distance above sample (7,000 nm). The effective Young's modulus was calculated using the Hertzian contact model by the Optics 11 Life data viewer software (version 2.3). Measurements without a contact point or with an otherwise unreliable model fit were regarded as false measurements and discarded from further analysis.

2.2.2.1. Turbidity assay. The gelation of the pre-gel PLECM and HLECM samples was determined with a turbidity assay. Cooled pre-gel solution (100 μl) was pipetted in a cooled 96-well plate (Greiner Bio one) and the plate was placed in infinite M nano plate reader (TECAN). The temperature was increased to 37 °C at the start of the assay. The absorbance was measured at 405 nm every 30s for 60 min. The normalized absorbance (N_A) was calculated using the following formula (1):

$$N_{A=}\frac{A(t)-A_0}{A_{max}-A_0} \quad (1)$$

Where A(t) is the measured absorbance at a time point, A_0 is the absorbance measured at time point T = 0 and A_{Max} is the maximum measured absorbance.

2.2.3. Scanning electron microscopy

LECM samples for scanning electron microscopy were fixed in 4% PFA and dehydrated in an ethanol/hexamethyldisilazane (Sigma) series, as previously described in Ref. [9]. The samples were coated in 15 μm gold (Quorum Q300T D sputtering device, Quorumtech) and scanned in a JSM-7500F field emission electron microscope (JEOL).

2.2.4. Organoid cultures

2.2.4.1. ICO initiation in BME. Viably frozen liver biopsies (N = 18) were partially thawed until a small ice clump containing tissue could be removed from the cryotubes. Tissue was washed in cold ADV+ (Table S2). Organoid initiation was performed as previously described [45]. In short, liver tissue was digested in 2.5 mg/ml Collagenase type A (Sigma) for 20 min at 37 °C. Afterwards, the suspension was strained (70 μm cell strainer) and washed with cold ADV+. The cell pellet was resuspended in reduced growth factor basement membrane matrix (BME, Cultrex) solution (70% BME, 30% cold ADV+). The cell suspension was plated in 25 μl droplets in 48-well suspension culture plates (Greiner Bio One). The BME was allowed to solidify for 45–60 min at 37 °C before 250 μl startup expansion medium (SEM, Table S3) was added. After 72 h, SEM was replaced with expansion medium (EM, Table S3).

ICO were cultured in BME according to previously published protocols [45]. EM was refreshed every 3–4 days and organoids were typically split every 7–10 days by mechanical dissociation. Organoid fragments were replated in fresh 25 μl BME droplets. Split ratios were empirically determined to maintain the 7–10 day ICO split schedule. Typically, ratios ranged from 1:4 to 1:8.

2.2.5. Transfer from BME to LECM hydrogel

ICO initiated in BME were transferred to LECM hydrogels after they were allowed to proliferate in BME for 2 passages. ICO were harvested by mechanical dissociation. Residual BME was washed away with cold ADV+ and centrifuged (453RCF, 4 °C). The resulting cell pellet was resuspended in cold LECM hydrogel. The cell-LECM suspensions were

plated in 25 μl droplets and were allowed to solidify at 37 °C for 45–60 min before 250 μl EM was added. Medium was refreshed every 3–4 days.

LECM grown ICO were split in a similar manner as BME-grown ICO. However, in case of dense 'cell-matrix' clumps, additional mechanical dissociation was performed in the well (after removal of EM and before collection in a cold 15 ml tube) or after the first wash and centrifugation step. In any case, mechanical dissociation was performed in small volumes (typically ranging from 100 to 500 μl) of cold ADV + using a 200 μl pipet by pipetting up and down until large fragments had been dissociated. The resulting ICO-fragment pellet was resuspended in LECM and plated in 25 μl droplets.

2.2.6. Live dead assay

Transferred ICO and ICO grown in BME were incubated with calcein AM (0.5 μM) and propidium iodide (50 μg/ml) at 37 °C, 5% CO_2 for 60 min. Afterwards, Hoechst 33342 (100 μg/ml) was added to stain all nuclei and incubated for 15 min. Organoids were imaged using an EVOS microscope (Thermofisher).

2.2.7. Cell proliferation assay

DNA synthesis, a hallmark for cell proliferation, was measured using a Click-iT™ EdU Cell Proliferation Kit (ThermoFisher). Experiments were performed in ICO 48 h after passaging. 5-ethynyl-2′-deoxyuridine (EdU, final concentration 10 μM) was added to EM and incubated at 37 °C for 4 h. Afterwards, ICO were harvested, made single cell using Trypsin-EDTA (15–30 min at 37 °C) and fixed/permeabilized using a Cytofix/Cytoperm kit (BD). The cells were fluorescently labelled with Alexa 488 according to the EdU protocol and the percentage of cells in S-phase was determined using a FACScanto II system (BD). Results were analyzed in Flowjo (10.7).

2.2.8. Metabolic assay

PrestoBlue assays were used to measure the increase in metabolic activity over time. ICO were plated in 48-well plates (n = 8 per condition). EM was replaced with 400 μl PrestoBlue solution (10% PrestoBlue in ADV+) and samples were incubated for 4 h at 37 °C. Empty hydrogel domes (HLECM, PLECM or BME) were included as negative background controls. After the incubation period, 3·100 μl was transferred to a white walled 96-well plate (Costar). Fluorescence intensity was measured using a fluorescent plate reader (ex:530 nm, em:590 nm). This was performed 1, 3, 5 and 7 days after plating ICO. The day 1 measurement was set as reference measurement for subsequent measurements.

2.2.9. Stable Isotope Labeling with amino acids in cell culture

Protein synthesis by the ICO was analyzed by labelling the proteins with Stable Isotope Labeling with Amino acids in Cell culture (SILAC). SILAC-R-Spondin medium was produced by replacing 'normal' L-Lysine with $^{13}C_6$ $^{15}N_2$ L-Lysine-2HCl and L- Arginine with $^{13}C_6$ $^{15}N_4$ L-Arginine-HCl. SILAC-R-Spondin was harvested, filtered and stored at −20 °C until used. SILAC-EM was prepared by replacing ADV+ and R-spondin with SILAC-ADV+ and SILAC-R-spondin containing 'heavy' amino acids. BME initiated ICO (N = 3) were cultured in 'heavy' EM for a minimum of 2 passages before ICO were switched to HLECM. Subsequently, ICO were cultured for another 3 passages before samples were harvested. All ICO were cultured for a minimum of 28 days in total in 'heavy' medium. Organoids were harvested by removal of medium and collection of the BME or HLECM domes. These were snap-frozen in liquid nitrogen and stored at −80 °C. Before analysis, samples were lyophilized (Zirbus Technology Sublimator 400).

2.2.10. Sample preparation

Lyophilized samples were rehydrated in 100–200 μl extraction buffer with 100 mM ammonium bicarbonate +8 M urea. Samples were homogenized using a Bioruptor®Plus (Diagenode SA) at 4 °C for 40 cycles, 15 s ON/OFF. This was followed by a centrifuge step (14,000 g, 15min) and the protein content of supernatants was determined using Pierce BCA Protein Assay Kit (Thermo Scientific). 30 μg of protein was processed further by reduction with 5 mM tris-2-carboxyethyl phosphine for 30 min at 37 °C and subsequently alkylated with 10 mM iodoacetamide for 45 min at RT. This was followed by overnight trypsin digestion at 37 °C. Digestion was stopped by addition of trifluoroacetic acid to a pH lower than 3. Desalting was performed using C18 reversed-phase spin columns (UltraMicro Spin Column, Nest group) according to manufacturer's instructions. After desalting, samples were resuspended in 2% acetonitrile and 0.1% trifluoroacetic acid. Peptide concentrations were determined using a NanoDrop 2000c (Thermo Scientific).

2.2.11. LC MS/MS analysis

The LC MS/MS analysis was performed on Tribrid mass spectrometer (MS) Orbitrap Fusion equipped with a Nanospray source and coupled with an EASY-nLC 1000 ultrahigh pressure liquid chromatography pump (Thermo Fischer Scientific). One microgram of peptide was loaded and concentrated on an Acclaim PepMap 100C18 precolumn (75 μm × 2 cm, Thermo Scientific) and then separated on an Acclaim PepMap RSLC column (75 μm × 25 cm, nanoViper, C18, 2 μm, 100 Å) with a column temperature of 45 °C. Peptides were eluted by a nonlinear 2 h gradient at the flow rate of 300 nl/min from 2% solvent B (0.1% formic acid/ACN, Merck)/98% Solvent A (0.1% formic acid in water, Merck) to 40% solvent B.

The Orbitrap Fusion was operated in the positive data-dependent acquisition mode. Full MS survey scans from m/z 375–1500 with a resolution 120,000 were performed in the Orbitrap detector. The automatic gain control target was set to 4×10^5 with an injection time of 50 ms. The most intense ions (up to 20) with charge states 2–7 from the full MS scan were selected for fragmentation. MS2 precursors were isolated with a quadrupole mass filter set to a width of 1.2 m/z. Precursors were fragmented by Higher Energy Collision Dissociation and detected in Orbitrap detector with the resolution of 30,000. The normalized collision energy in HCD cell was set 30%. The values for the automatic gain control target and injection time were 5×10^4 and 54 ms, respectively. The duration of dynamic exclusion was set 45s and the mass tolerance window 10 parts per million (PPM).

2.2.12. Data analysis

Analysis of raw files was performed with MaxQuant (version 2.0.1.0). The resulting peak lists were searched in Andromeda against a reviewed human UniProtKB database (release 2020_04), complemented with the standard MaxQuant contaminant database. Enzyme specificity was set to trypsin/P with a maximum of two missed cleavages. Precursor mass tolerance was set to 4.5 PPM and fragment ion mass tolerance to 20 PPM. Carbamidomethylation of cysteine was used as fixed modification and deamidation (Asparagine), oxidation (Methionine), hydroxyproline and acetylation were considered as variable modifications. The false discovery rate was set to 0.01 for both peptides and proteins, "match between runs" was enabled. Additional data analysis was done on LFQintensities in R (version 4.0.3). EdgeR (version 3.32.1) and Limma (version 3.46.0) R packages were used for differential expression analysis. The mass spectrometry proteomics data have been deposited to the ProteomeXchange Consortium via the PRIDE partner repository (ref: DOI: 10.6019/PXD028417).

2.2.13. ICO-initiation in LECM

Viably frozen biopsies (N = 21) were thawed and processed as described in 'ICO initiation in BME', however, one additional wash step was added after the collagenase step with PBS-EDTA (0.1 M) in order to stop collagenase activity. The resulting cell pellets were split two-way or three-way, depending on the size of the pellet. Large cell pellets were split three-ways (BME + PLECM + HLECM), whereas smaller pellets were split two-ways (BME + HLECM) or (BME + PLECM). The cell suspension was seeded in 25 μl domes and SEM was added after the hydrogel was allowed to solidify for 60 min at 37 °C. SEM was replaced 7 days after initiation with EM. Splitting of the cultures was performed as

previously described.

2.2.14. Differentiation of ICO

ICO grown in BME, transferred from BME to LECM and/or initiated in LECM were tested for their differentiation capacity towards hepatocyte-like cells. All ICO were differentiated after passage 4. The transferred ICO were cultured for 2 passages in LECM before the experiment was started. The differentiation experiment was performed as previously described for ICO grown in BME [10]. In short, the ICO were plated and cultured for 3–10 days in EM until LECM or BME (control) domes were 50–60% full. EM was replaced with EM + BMP-7 (25 ng/ml) and ICO were cultured for 5 more days. Afterwards, ICO were passaged according to normal procedure and differentiation medium (DM; Table S4) was added after hydrogel domes solidified. ICO were cultured for 9 days in DM before being harvested. Differentiated organoids were fixed in 4%PFA for histology or lysed and stored at −80 °C in Qiazol.

2.2.15. Large scale expansion in spinner flasks

The large scale expansion of ICO experiments were based on previously published methods by Schneeberger et al. [5]. The spinners were adapted for 50 ml conical tubes. ICO cultured in BME, transferred towards HLECM or initiated in HLECM were used for these experiments. ICO were cultured under normal conditions and expanded in EM. Harvesting of organoids was performed as described above. Single cell suspensions were created by incubation with Trypsin-EDTA for 15–20 min at 37 °C. BME (10%V/V) and HLECM (10%V/V) in EM suspensions were prepared on ice and mixed with cells. Starting concentration in the spinners was $1 \cdot 10^5$ cells/ml and starting volumes ranged from 2.5 ml to 5 ml. Cell + ECM extract suspensions were placed in 50 ml conical tubes and placed in an incubator (37 °C, 5% CO_2). ICO were incubated under constant rotation at 80RPM. EM + HLECM suspension was doubled every 3–4 days for a total of three times. On day 14, cells were harvested. The cell suspensions were homogenized by mechanical mixing and subdivided for further analysis. Cell suspensions (5 ml) were used for cell counting. Two times 5 ml of cell suspension was fixed in 4%PFA for histological analysis. An additional 5 ml of cell suspension was first centrifuged (480 g, 5min) before the cells were lysed in QIAzol and stored at −80 °C.

2.2.16. Histology

Samples were washed 3 times with 1x PBS before being permeabilized with 0.1% Triton-X-100 in 1x PBS for 20 min. The samples were blocked in 5% serum in 1x PBS for 60 min. The primary antibodies (Table S5) were incubated overnight at 4 °C. The samples were washed 5 times in 1x PBS before the secondary antibody (see Table S6) was added. The secondary antibody was incubated at RT for 60 min. Samples that were stained for cytokeratin 7 (KRT 7) or cytokeratin 19 (KRT 19) were stained with Alexa Fluor 488 Phalloidin (Thermofisher) for 20 min. All samples were stained with DAPI (Vectashield anti fade mounting medium with DAPI, Vectorlabs). Samples were imaged using a Leica 20X water dipping lens on Leica DM6000 CFS microscope with a LEICA TCS SP5 II confocal system. Data was processed and analyzed using ImageJ.

Formalin fixed paraffin embedded (FFPE) samples were sectioned as previously described (histology) at 4 μm. The sections were deparaffinized and heat-induced epitope retrieval was performed using TRIS-EDTA buffer (pH = 8.0). Slides were incubated in goat serum for 1 h before incubation of primary antibodies (see Table S5) overnight at 4 °C. Slides were washed using PBS before incubation (1 h, RT) with secondary antibodies (see Table S6). All slides were counterstained with DAPI (Vectashield anti fade mounting medium with DAPI, Vectorlabs), and imaged on a Leica DM6000 CFS microscope with a LEICA TCS SP5 II confocal system. Data was processed and analyzed using ImageJ.

2.2.17. RT-qPCR

Qiazol samples were homogenized using a TissueRuptor (Qiagen). RNA isolation was performed with the miRNeasy (Qiagen) kit according to manufacturers' protocol and RNA was measured on the Nanodrop 2000. cDNA (2 ng/μl) was prepared using 5x PrimeScript RT Master Mix and a 2730 Thermal cycler (Applied Biosystems). RT-qPCR was performed using SYBR select master mix for SFX (applied Biosystems) on a StepOnePlus RT PCR system (Applied Biosystems). Primers used are listed in Table S7.

2.3. Statistical analysis

Data analysis was performed in Prism 8.0. Kruskal-Wallis test by ranks was performed on data sets with non-paired samples or different samples sizes. Friedman test was performed on matched samples (stated in text).

3. Results

3.1. Characterization of liver extracellular matrix extract and hydrogel formation

LECM was obtained from fully decellularized human and porcine livers (Fig. 1A and Fig. S1) [9]. Complete decellularization of the livers was confirmed by histological evaluation (Fig. S1) and DNA quantification (Fig. 1B). To exclude potential zoonotic transmission of porcine endogenous retroviruses (PERV) [46], PERV-pol viral RNA was assessed in PLECM. As shown in Fig. 1C, no viral transcript was detected after decellularization, indicating that potential infectious retrovirus particles are effectively removed.

After pepsin-digestion, both PLECM and HLECM formed viscous suspensions (Fig. 1A) and during the normalization of pH to 7.5 (SD:± 0.1), the extracts formed stable hydrogels. The digestion efficiency (total protein content of supernatant compared to input weight of ECM) for PLECM was 40% (N = 8 pooled batches, SD:±5%) and 33% (N = 7 pooled batches, SD:±2%, Fig. 1D) for HLECM. Mass spectrometry analysis found 91 unique proteins for BME (supplementary file 1) and 17 for HLECM (supplementary file 1). For BME laminins are the most abundant proteins, whereas for the HLECM collagens were most abundant. There was an overlap of 5 proteins between BME and HLECM (Fig. 1E). No significant differences in amount of total collagen were found between PLECM and HLECM hydrogels (Fig. 1F). Compared to commercially available Matrigel (Corning) and BME (Cultrex), LECM was found to contain 43 and 86 times more total collagen, respectively. IHC staining for collagen type I, III and IV showed that all three types were present in the LECM hydrogels (Fig. S1). No significant differences in sGAG content between LECM (average HLECM: 36 μg/mg protein, SD: ±6 μg/mg protein, N = 4 different batches, PLECM: 44 μg/ml protein, SD:±7 μg/ml protein, N = 4 different batches) and BME (BME: 37 μg/mg, N = 1 batch, Matrigel: 48 μg/mg, N = 1 batch) were found (Fig. 1G). The turbidity assay revealed that PLECM has a longer lag-phase before turbidity increased (Fig. S1). The pooled batches of HLECM (N = 3) reach $T_{1/2}$ on average after 20 min and PLECM (N = 3) after 30 min, but both LECM extracts preparations plateau off at the same time. This could indicate that the pepsin extrication reduced the PLECM into smaller fragments than HLECM [47].

The mechanical hydrogel characteristics were determined by shear rheology and nanoindentation measurements. Average peak values for the storage modulus (G') measured during a time sweep indicate that PLECM (3.0 mg/ml) has a higher stiffness when compared to Matrigel and HLECM *using* (3.0 mg/ml) (Fig. 1H). Stiffness of PLECM was significantly different from Matrigel ($P < 0.05$), but did not significantly differ from either Matrigel or HLECM. Representative examples of frequency, shear and time sweeps for different LECM formulations are shown in Fig. S2. Nano-indentation experiments revealed no significant differences between pooled batches of PLECM (315Pa, SD:±203Pa) and HLECM (322Pa, SD:±204Pa) when comparing effective Young's modulus (Fig. 1I). Matrigel (612Pa, SD:±57Pa) did have a significantly

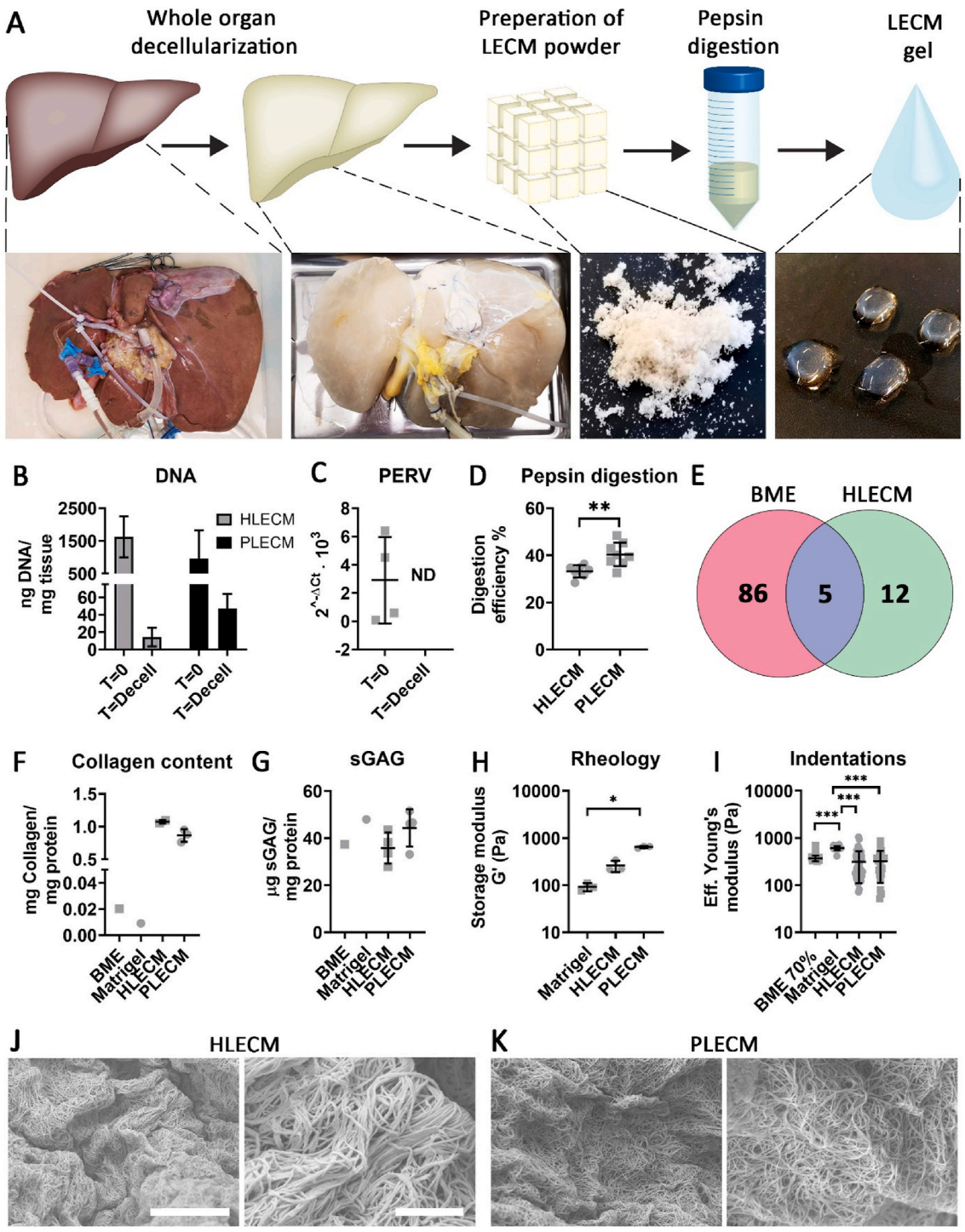

Fig. 1. Preparation and characterization of LECM extracts from decellularized livers. A: Schematic overview showing the entire process from liver decellularization, preparation of lyophilized LECM powders and extraction of LECM pepsin digestion. B: Confirmation of full cell removal in both porcine and human livers. DNA concentration after decellularization was 47.2 ng DNA (N = 8, SD:±15.4 ng) for porcine livers and 14.3 ng DNA (N = 4, SD:±9.2 ng) for human livers. C: Removal of PERV from porcine livers was confirmed using qPCR methods. No PERV was detected after decellularization (N = 4). D: The digestion efficiency of the LECM as determined by the amount of input material and measured protein content afterwards. The difference in digestion efficiency between PLECM (average: 40%, SD: ±5%) and HLECM (average: 33%, SD:±2%) was significant ($P < 0.01$, N = 8 different pooled batches of HLECM and PLECM) and PLECM was digested more efficiently than the human ECM. E: Venn diagram showing the number of unique proteins found for BME and HLECM. 5 overlapping proteins were found. F: Total collagen content of different substrates showing that LECM (PLECM: 0.9 mg collagen mg^{-1} protein, SD: ±0.13 mg, N = 3 pooled batches, HLECM: 1.0 mg, SD:±0.24 mg, N = 2 pooled batches) contained more collagen than commercially available BME (N = 1). G: No significant differences were found between BME (N = 1) and LECM (PLECM and HLECM; N = 4) for the total sGAG content after solubilization. H: max storage modulus (G′) values measured by rheology. The difference between matrigel (N = 3, average: 92Pa, SD:±15Pa) and PLECM (N = 3, average: 647Pa, SD:±30Pa) was significant ($P < 0.05$). PLECM has a higher G′ than HLECM (N = 3, average 260Pa, SD:±57Pa). I: Nano-indentation showed that matrigel (average: 612Pa,SD:±57Pa) had a significantly higher (P,0.001) effective Young's modulus than BME 70% (average:371Pa,SD:±50Pa), HLECM (average:315Pa,SD:203Pa) and PLECM (average:322Pa, SD:±204Pa). IJ: scanning election microscopy images for HLECM (I) and PLECM (J) showing the fibrous structure of the LECM hydrogels. Scale bars (from left to right): 10 µm, 2.2 µm, 10 µm and 5 µm).

higher Young's modulus (P < 0,001) than both LECM preparations and BME 70% (371Pa, SD:±50Pa). LECM hydrogels prepared from individual livers showed significant biomechanical heterogeneity between individual livers, in both PLECM (n = 4) and HLECM (n = 4) (Fig. S1). PLECM extract for porcine liver 1, liver 1 had significantly higher (P < 0.0001) effective Young's modulus compared to the other three porcine livers. Significant differences were also determined between human liver 2 and 3 and human liver 3 and 4 (both p < 0.01). This unwanted heterogeneity can be mitigated by pooling extracts of multiple livers together.

Increasing the concentration of the PLECM and HLECM hydrogels (6 mg/ml) did not yield higher effective Young's modulus (Fig. S2), which indicates less efficient solidification of the LECM hydrogels at higher concentrations. At lower concentrations, the resulting hydrogel domes were difficult to reliably measure using the Nanoindenter, as finding the surface, which is required for the Hertzian contact model, was challenging. No significant differences were found between PLECM and HLECM of similar (6.0 mg/ml and 4.5 mg/ml) concentrations (Fig. S2).

Scanning electron microscopy showed the fiber structures within HLECM (Fig. 1J) and PLECM (Fig. 1K). No clear differences were observed, with both hydrogels showing non-aligned bundles of fibers present within the overall structure.

Matrix-bound growth factors can influence cell behavior. Forty different growth factors were quantified in order to determine the effect of decellularization and solubilization. Thirty-three (out of 40) human growth factors were detected in human liver samples before decell (T = 0). In general, the concentration of growth factors decreased after decellularization and remained stable during the solubilization process (Fig. S2, relative change compared to T = 0).

3.2. Transfer of ICO from BME to PLECM hydrogels

To determine the optimal PLECM concentration, ICO were transferred from BME to different concentrations of PLECM hydrogel (4.5 mg/ml, 3 mg/ml and 1.5 mg/ml, Fig. 2A). Bright field microscopy examinations of ICO cultures in BME and PLECM at day 3 and day 7 showed that organoid growth was maintained in PLECM hydrogels (Fig. 2B). ICO altered the shapes of the.

PLECM domes, forming dense aggregates that came off from the well surface, as was especially evident at the lowest (1.5 mg/ml) PLECM concentration, demonstrating ECM-remodeling. PLECM domes at 3 mg/ml and 4.5 mg/ml were more stable over the culture period. The ICO created small branch-like structures or formed tube-like structures inside the PLECM in all concentrations (Fig. S3). Similar structures were not seen in BME controls.

Passaging of ICO grown in LECM was done using the standard passaging protocol. However, dissociation of dense aggregates into smaller fragments required more mechanical dissociation by pipetting up and down when compared to BME controls. Especially ICO grown in the condensed 1.5 mg/ml and stiffer 4.5 mg/ml conditions were more difficult to dissociate. This caused uneven spread of cells through fresh PLECM and subsequently, uneven organoid growth. The 3 mg/ml PLECM contained fewer dense organoids structures and could therefore be mechanically dissociated more easily than the other conditions.

Switching ICO from BME to PLECM hydrogels did not change the gene expression (N = 9) of selected genes (Fig. 2C, Fig. S3). Also no major differences in protein expression of KRT-7, a cholangiocyte marker, and albumin, a marker for hepatocyte-like cells, were observed for ICO grown in PLECM (Fig. 2D).

The changes in optical density as a result of ICO-ECM interactions when grown in PLECM were typically visualized as 'pulling' on the PLECM fibers. This interaction alters the biochemical and physical characteristics of the local environment surrounding the organoids, which could mitigate the effects of different PLECM concentrations. The PLECM 3.0 mg/ml condition was chosen as the optimal culture condition for expansion of ICO, also partly based upon ease-of-use, since this ICO grown in this concentration required less mechanical dissociation than the 1.5 mg/ml or 4.5 mg/ml.

Cell viability is a common issue in the field of liver tissue engineering. However, Huch et al. showed that ICO can be maintained *in vitro* for up to 6 months in BME [1]. The transfer from BME to PLECM could influence the cell viability, and therefore a live dead assay was performed to assess cell viability after transferring to PLECM. Fig. 2E shows representative images of ICO grown in BME and transferred to 3.0 mg/ml PLECM. Viable cells converted calcein AM to fluorescent (green) calcein and dead cells were stained with propidium iodide.

3.3. Transfer of ICO from BME to HLECM hydrogels

Transfer experiments were extended to HLECM hydrogels (N = 3, Fig. S3), with generally similar results to PLECM hydrogel cultures. As 3 mg/ml HLECM performed similarly to 3 mg/ml PLECM this concentration was also chosen to culture ICO. At 3.0 mg/ml, protein expression of KRT-7 and albumin (Fig. 3B) was similar when grown in BME (Fig. 3A). Expression of zonula occludens 1 (ZO-1) was also similar for ICO grown in BME or ICO transferred to HLECM or PLECM (Fig. 3B). There were no significant differences in gene expression of selected genes between ICO grown in BME (N = 16), HLECM (N = 10) or PLECM (N = 10, Fig. 3C, Fig. S3).

ICO were passaged every 7–10 days. In general, ICO transferred towards LECM hydrogels were split in lower ratios (30–50% lower) than their control counterparts grown in BME, which indicates lower proliferation rates. However, after 7 days of culture, no significant differences were found in gene or protein expression of the proliferation marker KI-67 (Fig. 3D and 3E) between the ICO grown in different substrates.

EdU incorporation was performed two days after passaging in order to determine the amount of cells that synthesize *de novo* DNA in the S-phase during a 4-h incubation period. ICO grown in BME showed the highest percentage of proliferating cells (average:11.9%, SD:±4.9%, Fig. 3F). The difference between BME and HLECM (average: 6.2%, SD: ±4.4%) was significant (P < 0.05), whereas the difference between BME and PLECM (average: 6.1%, SD:±3.4%) approached significance (P = 0.06). ICO grown in HLECM or PLECM also had lower metabolic activity over a 7-day culture period, which was on average 1.8-fold lower when compared to BME (N = 11 for BME and PLECM, N = 5 for HLECM, Fig. 3G). This difference was, however, not significant at the day 7 time point.

3.3.1. Proteome analyses of ICO cultured in BME and HLECM

Cells are capable of responding to changes in their local environment and can do so by altering the syntheses and turnover of proteins. Normal mass spectrometry (MS) techniques are limited in detecting these (often subtle) changes, as the *de novo* synthesized proteins can be obscured by the large bulk of pre-existing proteins (e.g. ECM components from the culture substrates). However, Stable Isotope Labelling with Amino acids in Cell culture (SILAC) allows for labelling of the synthesized proteins by replacing amino acids with normal-weight isotopes with amino acids with heavy-weight isotopes (Fig. 4A). SILAC was used to determine the proteins produced by ICO that were initially cultured in BME and transferred to HLECM.

In total, 2,184 unique heavy-weight' proteins produced by ICO were identified. On average, 665 proteins (SD:±96 proteins) could be detected which were synthesized by ICO grown in BME (N = 3). For the ICO transferred to HLECM, 672 synthesized heavy-weight proteins (SD:±152 proteins) were detected. Out of these proteins, on average 620 proteins (SD:±95 proteins, BME) and 629 proteins (SD:±150 proteins, HLECM) were identified as cellular proteins. The remaining 45 (BME) and 43 (HLECM) proteins were identified as proteins related to the ECM (Fig. 4B). Interestingly, in the collagen-based HLECM more heavy collagens were found. In the laminin-based BME more proteoglycans were found. This indicates that the culture substrate influences the proteins produced by the cells. Of all detected proteins, 373 proteins were

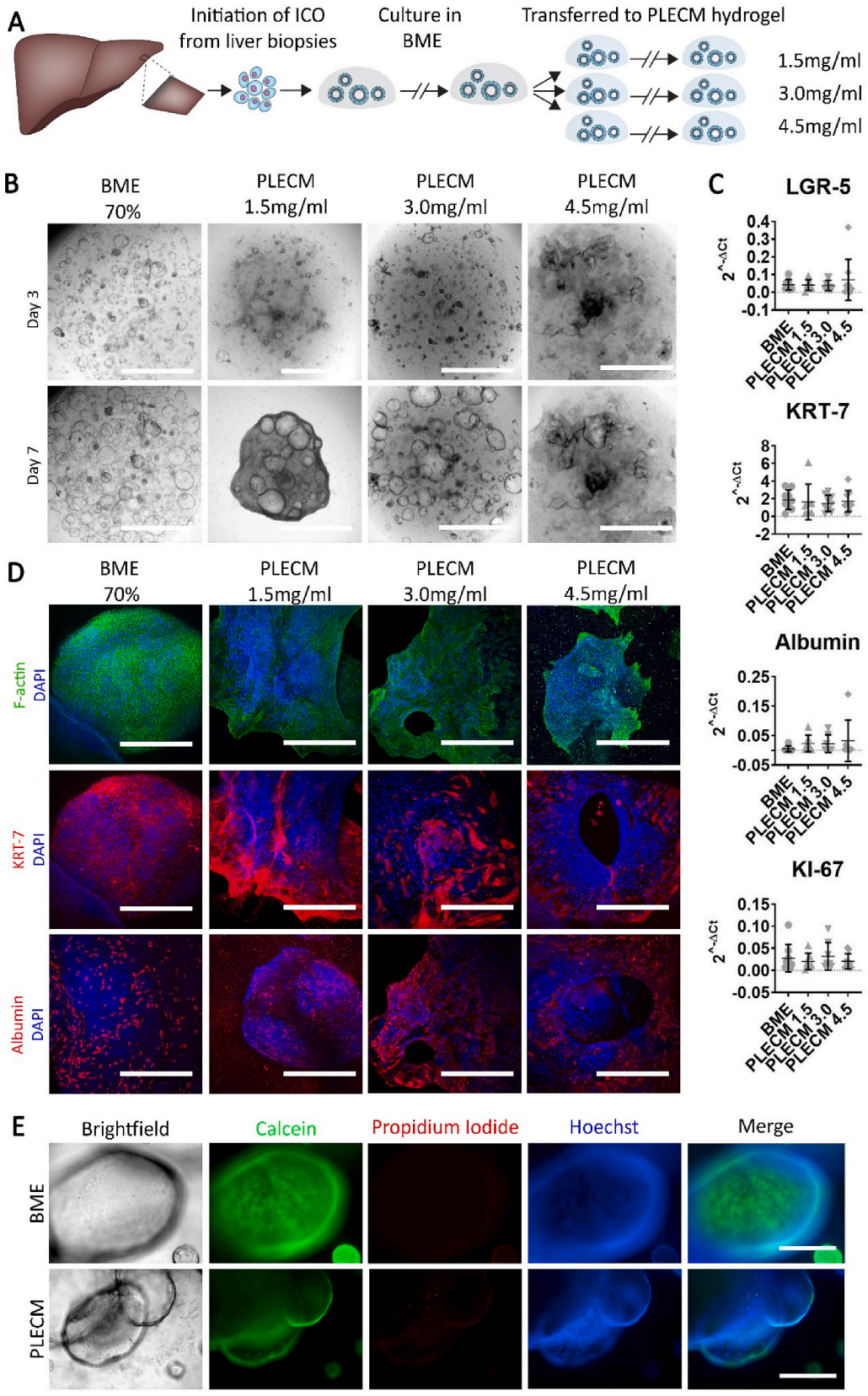

Fig. 2. ICO can successfully be cultured in PLECM hydrogels. A: schematic representation for initiation of ICO from liver biopsies in BME and subsequent transfer towards PLECM hydrogels of various concentrations. B: Bright field images of organoids growth in BME and various concentrations PLECM at day 3 (top row) and day 7 (bottom row). Scale bars: 2000 μm. C: gene-expression (2-ΔCt) of selected genes show no significant differences between ICO grown in BME and varying concentrations of PLECM. D: F-actin, KRT-7 and Albumin were expressed in ICO grown in BME and varying concentration of PLECM. Scale bars: 200 μm. E: Representative images of live dead staining of ICO grown in BME and ICO transferred to PLECM. Calcein (green) represents live cells and propidium iodide (red) dead cells. Scale bars: 400 μm. (For interpretation of the references to color in this figure legend, the reader is referred to the Web version of this article.)

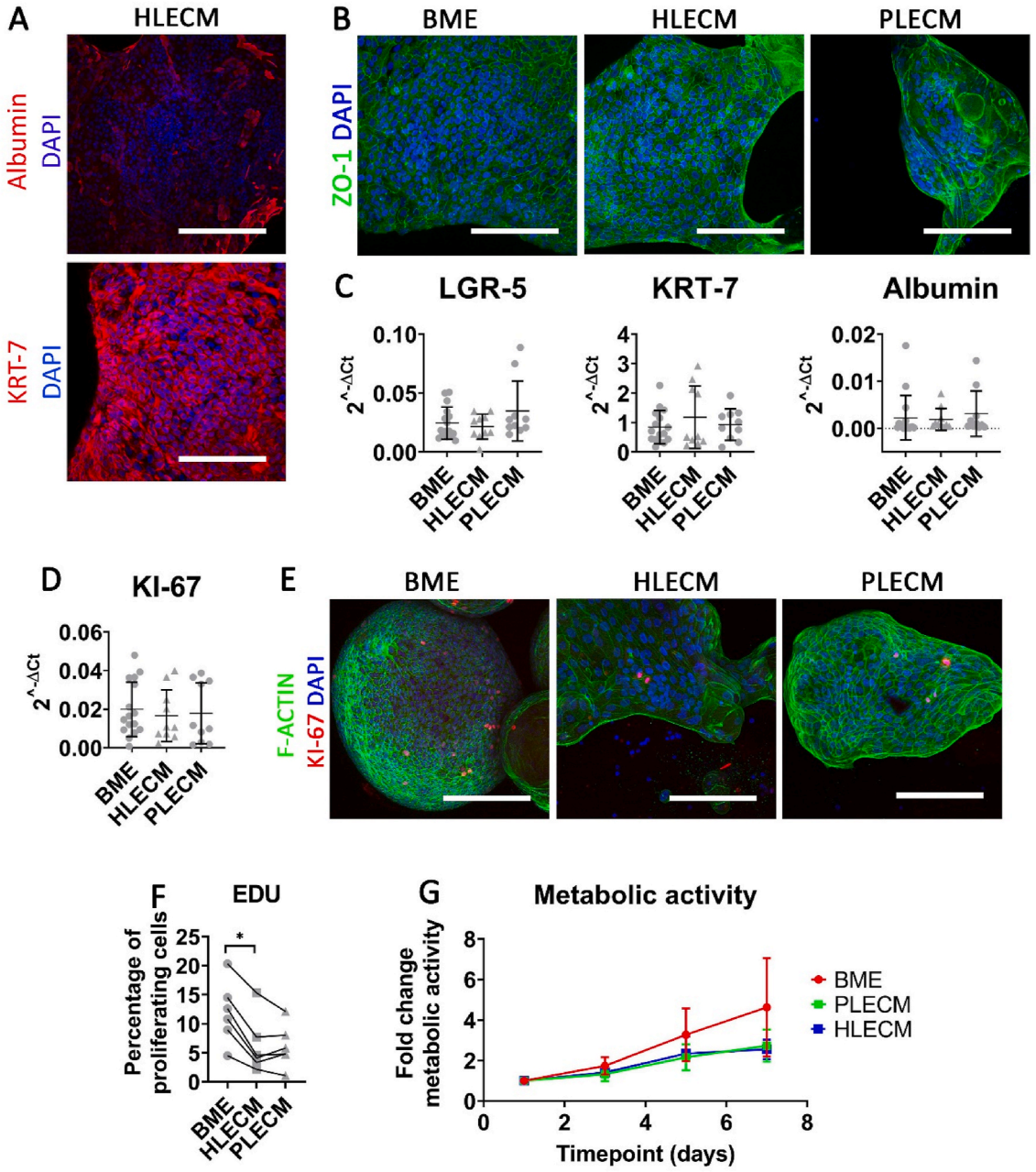

Fig. 3. Switching from BME to LECM hydrogels does not significantly alter ICO gene expression, but does lower proliferation rates. A: ICO transferred towards HLECM maintained expression of Albumin and KRT. Scale bars: 100 μm. B: Transferred organoids (HLECM and PLECM) maintained expression of ZO-1. Scale bars: 100 μm. C: Gene expression (2-ΔCt) does not show significant differences between ICO transferred to HLECM (N = 10) or PLECM (N = 10) and BME controls (N = 16) for selected genes. D: Gene expression (2-ΔCt) does not reveal significant differences after 7 days of culturing ICO in LECM. E: Each ICO contained several nuclei positive for the proliferation marker KI-67. Scale bars: 100 μm. F: EDU incorporation (N = 6 matched ICO pairs) reveals that ICO grown in BME (12%, SD:±5%) had significantly more proliferating cells compared to HLECM (6%, SD:±4%, $P < 0.05$), but not to PLECM (6%, SD:±3%, P = 0.06). G: relative metabolic activity over a 7-day period as measured by PrestoBlue reveals BME (N = 10) had higher metabolic activity than PLECM (N = 5) and HLECM (N = 5). Fold change was calculated based upon day 1 activity for each sample.

present in both groups. When looking more closely at these 373 proteins, no differentially expressed proteins could be found (Fig. 4C), indicating no significant changes in synthesized proteins by the ICO upon changing from BME to HLECM. However, subtle differences were present. Proteins, such as CA-2 and HNRNPM, were more abundant in HLECM. CA-2 plays a role in acid base homeostasis [48]. HNRNPM plays a role in RNA splicing [49] and was closest to differentially expressed for the HLECM group. Simultaneously, there were also proteins which were more abundant in BME. These were for example HSPG2 (Perlecan), IQGAP-1 and RPL7A. Perlecan is a component of basement membranes [13,14] and IQGAP-1 is a regulator molecule in bile canaliculi [50]. RPL7A was closest to being differentially expressed for the BME grown ICO. In other words, subtle non-significant differences exist for proteins produced by ICO grown in both substrates. Ten proteins were exclusively present in BME grown ICO, but not in ICO transferred to HLECM. Proteins are classified as exclusive if they are present in all samples of one conditions, while absent in all others. These proteins are listed in supplementary file 1. Vice versa, ten proteins were exclusively found in ICO transferred to HLECM. Interestingly, six out of ten protein exclusively found for HLECM are collagens, whereas three out of ten exclusive proteins for the

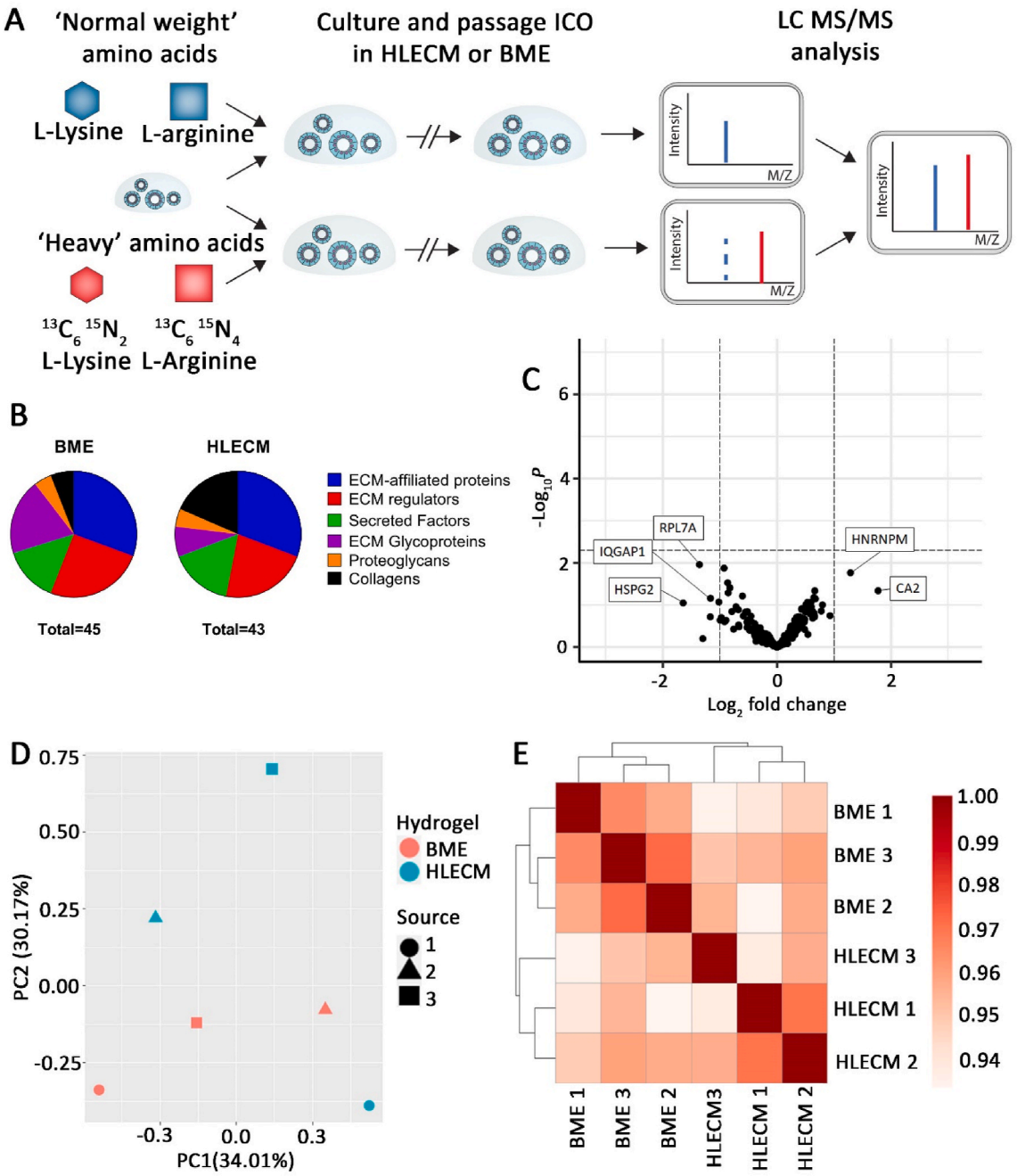

Fig. 4. SILAC assessment does not reveal significant differences in proteins synthesized by ICO grown in BME or HLECM. A: schematic overview of SILAC experiments. EM was replaced with 'heavy' medium containing L-Lysine and L-arginine with heavier isotopes. ICO were cultured for 2 passages in heavy EM in BME before they were transferred towards HLECM and cultured for another three passages. B: 45 and 43 matrisome-related proteins were detected for BME and HLECM grown ICO respectively. C: Volcano plot showing that there were no differentially expressed proteins present in all samples. D: Principal components analysis does not reveal any clustering based on donor and/or matrix in which ICO were grown. E: The heat map shows that samples can cluster based upon culture substrate.

BME group are glycoproteins related to the basement membrane. This could indicate that cells respond to the biochemical differences in their environment.

A PCA plot of all protein abundances shows a heterogeneous production of proteins in each group, with no apparent clustering of organoid lines or culture substrates (HLECM or BME) (Fig. 4D). The samples do cluster together based on culture substrate based on subtle differences in protein abundances between the BME or HLECM group (Fig. 4E). Taken together, the data shows that subtle differences exist in proteins synthesized by ICO when cultured in BME or HLECM, but no significant differences were found.

3.4. Direct initiation of ICO cultures in LECM

Previous experiments were performed with ICO initiated in BME as per normal initiation protocol. However, for clinical applications, a mouse tumor-derived BME free culture is required. Therefore, it was investigated whether ICO could also be initiated in LECM hydrogels. In order to do so, the cell suspension for ICO initiation was divided in equals parts and cultures were initiated in LECM hydrogels.

During the first days of culture, small cyst-like organoids became visible. Typically, there were less ICO present in HLECM (Fig. 5B). The BME cultures, which were deemed successful, were split 7–10 days after initiation, whereas the HLECM cultures were typically split for the first

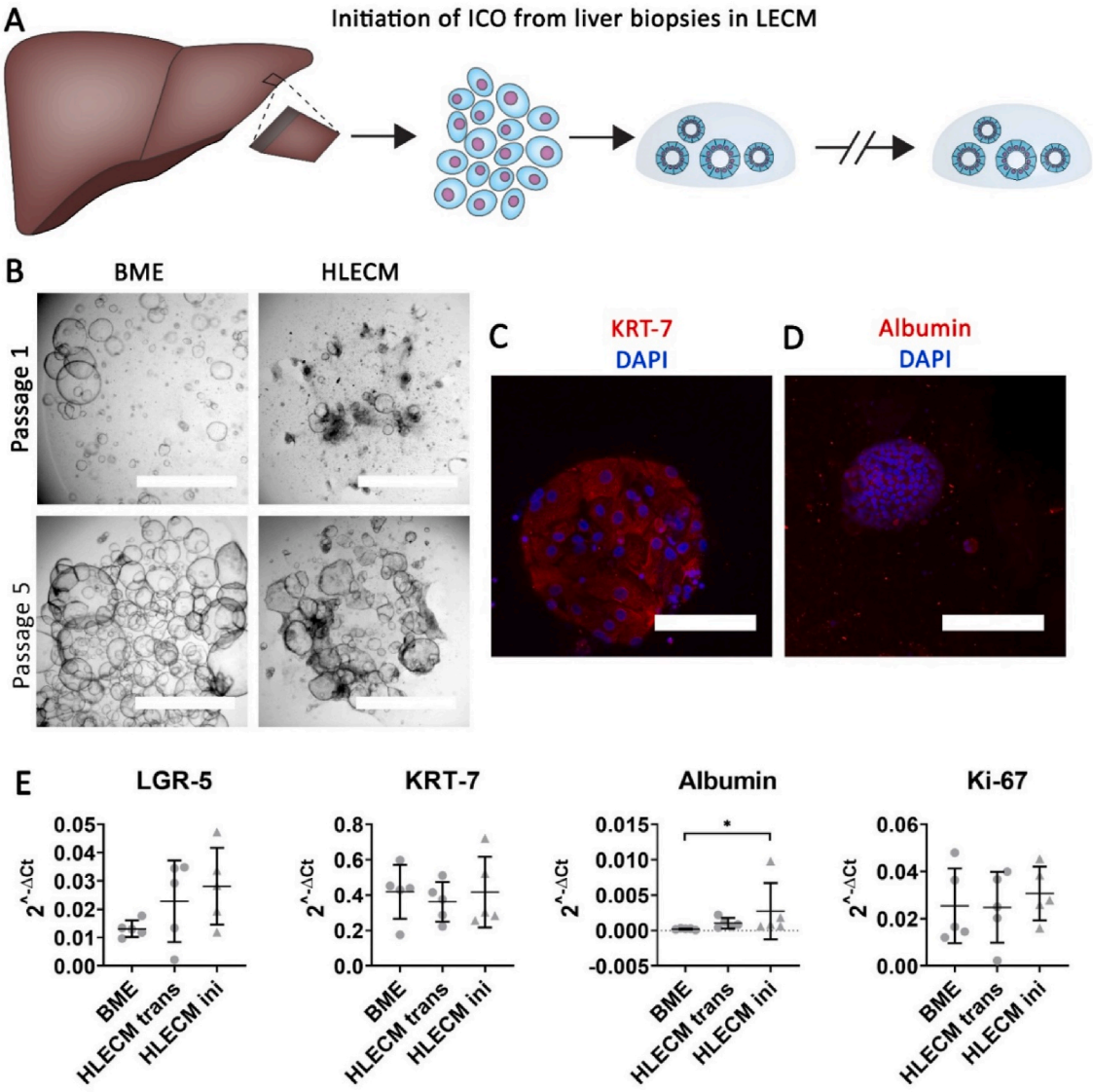

Fig. 5. ICO could successfully be initiated in LECM. A: A schematic overview of the initiation of ICO from liver biopsies in HLECM. B: Representative bright field images of ICO cultures deemed successful at passage 1 and 5 (scale bar: 2,000 μm). CD: Whole mount confocal images for KRT-7(C) and albumin (D). Scale bars: 100 μm (C) and 200 μm (D). E: Gene expression (2-ΔCt) of selected genes between matched ICO from the same donors (N = 5) grown in BME (BME), ICO transferred from BME towards HLECM (HLECM trans) and initiated in HLECM (HLECM ini). Significant differences were found for albumin between BME and HLECM ini ($P < 0.05$).

time after 14 days. This indicated that ICO initiated in LECM grew slower than their BME counterparts. Out of all initiated cultures, 63% of HLECM initiated ICO and 67% of the PLECM initiated ICO were deemed as successful cultures. For BME initiated organoids this percentage was 74%. A successful culture was defined by the presence of multiple (>10) ICO per dome, which could be expanded within 14 days. The ICO initiated in LECM had phenotypes similar to BME grown ICO or ICO transferred to LECM (Fig. 5B, Fig. S4).

The ICO initiated in LECM showed similar proliferation patterns as matched BME-to-LECM transferred ICO and were split in similar ratios. In general, proliferation rates were lower in HLECM, but large donor variations were noted with some individual ICO lines growing at the same pace as their BME initiated counterparts. Moreover, ICO could be maintained for 10 passages (Fig. S4). Expression of F-actin (HLECM initiated ICO: Fig. S4B, PLECM initiated ICO: Fig. S5) was comparable between BME grown ICO and ICO transferred from BME to LECM hydrogels. Moreover, KRT-7 and Albumin protein expression was visualized by whole mount confocal staining (HLECM initiated ICO: Fig. 5CD, PLECM initiated ICO: Fig. S5). On gene expression level a significant difference in albumin expression ($p < 0.05$) was found between matched (N = 5) BME grown and HLECM initiated ICO (Fig. 5E). Expression of albumin was on average 12-fold (SD:±14) higher compared to ICO grown in BME. Other than that, no significant differences were found for the selected genes for HLECM initiated ICO (Fig. 6E) and PLECM initiated ICO (Fig. S5). Overall, this indicates that ICO initiated in HLECM and PLECM were able to proliferate, and retain a similar overall phenotype and gene expression levels as BME initiated ICO.

3.4.1. *ICO differentiation towards hepatocyte-like cells*

ICO can be stimulated to differentiate towards hepatocyte-like cells when cultured in differentiation medium (DM; Fig. 6A) [1]. However, these differentiation protocols are not optimal yet as no mature hepatocytes in terms of hepatocyte functionality and/or expression of hepatocyte markers are grown [10]. Tissue-specific micro-environments have shown to aid and/or improve the differentiation of (induced) pluripotent stem cells towards hepatocyte(-like) cells [51–53]. Therefore, ICO were differentiated to test whether tissue-specific LECM can

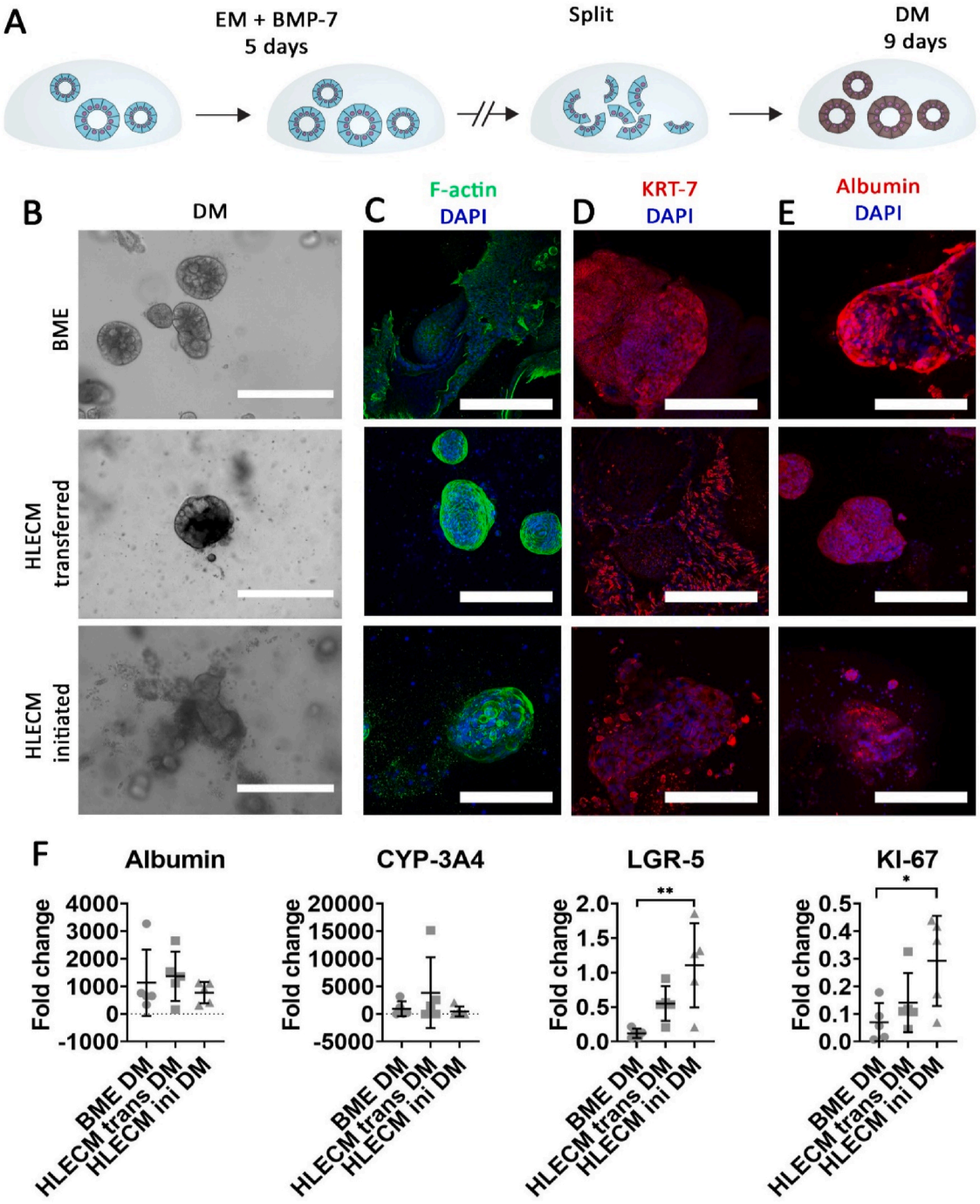

Fig. 6. The use of tissue-specific HLECM extracts did not aid in the differentiation of cholangiocytes towards hepatocyte-like cells. A: Schematic for the differentiation protocol. The ICO were first grown in EM for 4–10 days (not shown), before medium was supplemented with BMP-7 for 5 days. The ICO were split once before medium was switched to differentiation medium. B: Bright field images showing ICO on day 9 of being cultured in DM. ICO were growing in dense structures and were smaller than their EM-control counterparts. Scale bars: 200 μm. CDE: whole mount confocal images for F-actin (C), KRT-7(D) and albumin(E) of differentiated ICO. Scale bars: 200 μm. F: Fold changes (2-ΔΔCt) of selected genes compared to matched ICO grown in BME in EM. Albumin and CYP-3A4 were upregulated when compared to the BME grown ICO control, whereas LGR-5 and KI-67 were downregulated. LGR-5 and KI-67 was significantly (LGR-5: $P < 0.01$, KI-67: $P < 0.05$) higher for ICO initiated in HLECM when compared to BME grown ICO.

improve the differentiation towards hepatocytes.

Concentration series (1.5 mg/ml, 3.0 mg/ml and 4.5 mg/ml) with ICO transferred from BME to PLECM (N = 9) were first performed in order to establish the effect of differences in (bio)physical characteristics. ICO became dense in structure and had smaller lumens (Fig. S6). Moreover, F-actin expression of cells changed from a more 'honey comb'-like structure in EM to random deposition of F-actin in DM (Fig. S6). Gene expression of hepatic markers, such as albumin, CYP-3A4, HNF-4α and.

MRP-2, were upregulated upon differentiation. KI-67 and LGR-5, markers for proliferation and stem-cell phenotype, expression was downregulated, whereas, KRT-7 and KRT-19 expression remained stable (Fig. S6). However, no significant differences were found between BME grown ICO or ICO transferred to PLECM or between the different PLECM concentrations.

These differentiation experiments were repeated with ICO

transferred towards HLECM and ICO initiated in HLECM. Experiments were performed with N = 5 sets of ICO at a HLECM concentration of 3.0 mg/ml. Upon differentiation, the ICO form relative small and optically more dense 'clump' of cells (Fig. 6B). HE-staining revealed that these differentiated ICO often have multiple lumens (Fig. S7). Expression patterns of F-actin changed from 'honey comb'-like structures in EM to more randomly deposited patterns in DM, similar to PLECM initiated ICO (Fig. 4C).

The cholangiocyte marker KRT-7 was still detectable in all conditions after differentiation (Fig. 6C). Albumin staining was also detectable in all conditions. Increase in albumin expression was observed on gene expression level, as 1,136-fold (SD:±1,078-fold), 1368-fold (SD:±801-fold) and 774-fold (SD:±344-fold) increases were calculated for the ICO grown in BME, ICO transferred towards HLECM and ICO initiated in HLECM, respectively, compared to BME grown ICO controls. Similarly, CYP-3A4 was upregulated 945-fold (SD:±1205-fold) for the BME grown ICO, whereas the expression ICO transferred towards HLECM was upregulated 3853-fold (SD:±5731-fold) compared to BME controls. Expression of CYP-3A4 was 476-fold (SD:±808-fold) higher for the ICO initiated in HLECM compared to BME controls. However, the differences between conditions were not significant. Gene expression of LGR5-5 ($P < 0.01$) and KRT-7 ($P < 0.05$) did significantly differ between BME

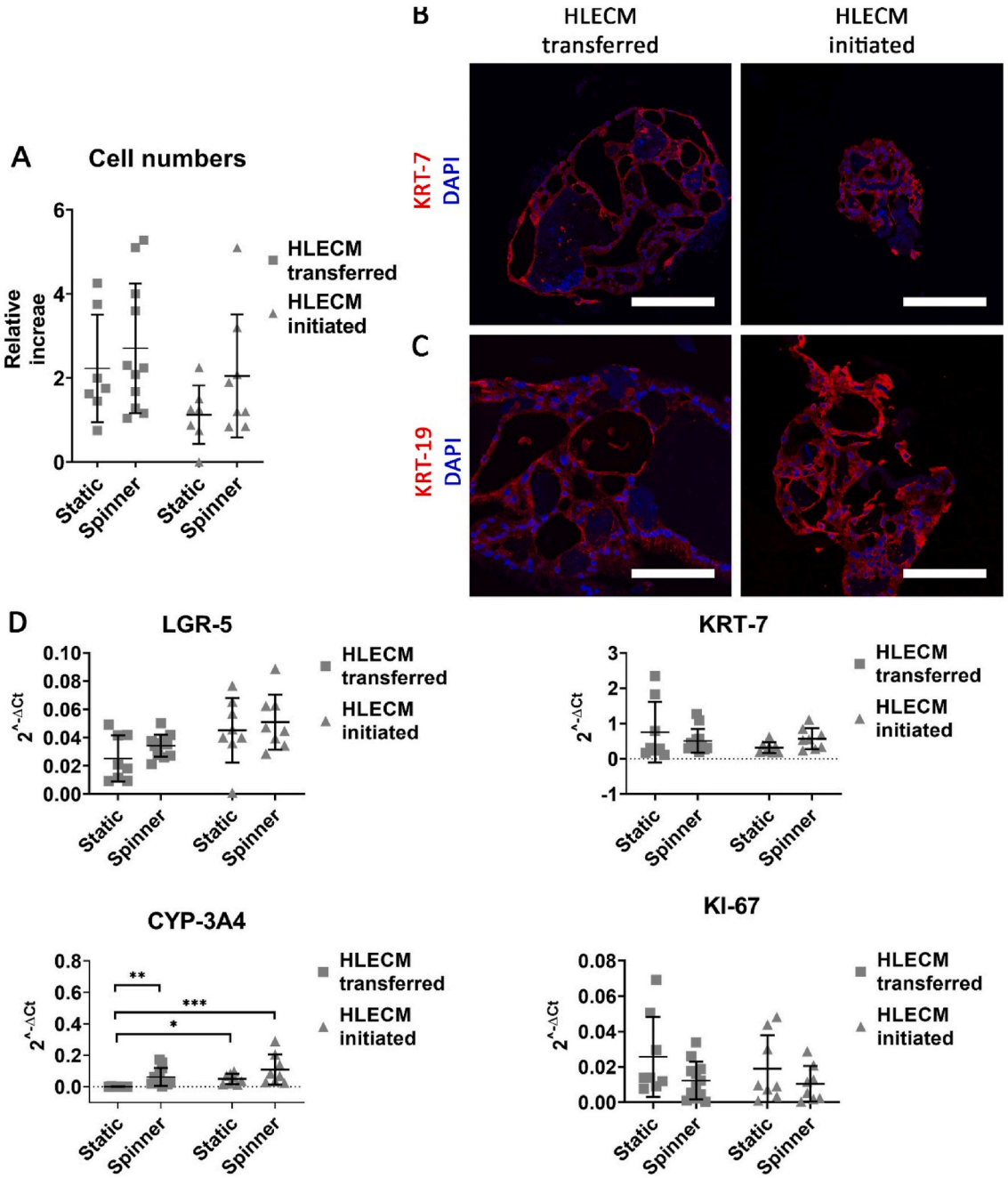

Fig. 7. Large-scale expansion of ICO using spinner flasks is feasible. A: The relative increase in cell numbers after 14 days of culture compared to T = 0. ICO transferred to HLECM increased 3-fold (SD:±1-fold) and ICO initiated in HLECM 2-fold (SD:±1-fold). The difference was not significant. The respective static controls increased 2-fold (Transferred to HLECM, SD:±1-fold) and 1-fold (initiated in HLECM, SD:±1-fold). BC: Immunofluorescence of PPFE slides stained for KRT-7 (B) and KRT-19 (C). Scale bars: 200 μm (B) and 100 μm (C). D: Gene expression of selected genes between ICO expanded in spinner flasks and ICO grown in static hydrogel domes. No significant differences were found for LGR-5 and KRT-7, whereas ICO had higher expression of CYP-3A4 when cultured under dynamic spinner conditions compared to static controls (*:$P < 0.05$, **:$P < 0.01$, ***: $P < 0.001$). No significant differences were found for KI-67 expression.

grown ICO and ICO initiated in HLECM. Significant differences were also found for expression of HNF-4α and KRT-19 between BME grown ICO and ICO transferred towards HLECM (Fig. S7, $P < 0.05$). HLECM initiated ICO can be differentiated towards hepatocyte-like cells with comparable efficiency as their BME grown counterparts.

3.4.2. Dynamic expansion of ICO in HLECM

TERM applications, such as repopulation of damaged or decellularized biliary tree with cholangiocytes, require large numbers of viable cells. Current static culture techniques are inefficient and time-consuming. Moreover, they are prone to pipetting errors, leading to loss of cells or contamination of cultures. Schneeberger et al. showed that dynamic cultures in spinner flasks allow for safe, convenient and large scale expansion. This protocol was adapted for use with 50 ml conical tubes in order to test whether HLECM can be used for this dynamic and easy form of organoid expansion. Experiments were performed with HLECM initiated organoids ($N = 8$) and BME-to-HLECM transferred organoids ($N = 12$). Small spherical organoids started becoming visible after an initial lag-phase of three days. The ICO appeared to 'clump' together into large and heavy aggregates, which sunk to the bottom of the spinners. The relative increases in cell numbers after 14 days of culture compared to the start were 3-fold (SD:±1.5) for the ICO transferred to HLECM and 2-fold (SD:±1.4) for the ICO initiated in HLECM (Fig. 7A). On average the spinners yielded more cells than the static controls, as the cell numbers in static controls only increase 2-fold (ICO transferred to HLECM, SD:±1.2) and 1.1-fold (ICO initiated in HLECM, SD:±0.6). ICO transferred from BME to HLECM or initiated in HLECM were growing on denser structures (Fig. S8). HE-staining of FFPE-sections revealed that the ICO were growing on HLECM particles in the suspension (Fig. S8). ICO were positive for KRT-7 (Fig. 7B) and KRT-19 (Fig. 7C).

Gene expression of selected genes showed a trend to express higher levels of LGR-5 in the spinners, but differences were not significant (Fig. 7D). Similarly, no significant differences could be found for expression of KRT-7, LGR-5 or KI-67. Interestingly, expression of CYP-3A4 was upregulated under dynamic spinner conditions. The expression was on average 66-fold (transferred) and 2.2-fold (initiated) higher under dynamic conditions when compared to their respective static controls. No significant differences were found between KRT-19 and albumin (Fig. S8). Expression of HNF-4α remained stable between the three spinner conditions, whereas MRP-2 was upregulated for the BME grown ICO spinner condition (Fig. S8). These results show that LECM can also be used for more efficient expansion of ICO in a clinically relevant manner, as the cell yield can be doubled under dynamic culture conditions.

4. Discussion

Patient-derived hepatobiliary organoids are a promising cell source for clinically relevant TERM applications. However, the mouse tumor-derived ECM extracts that are typically used to initiate and expand these organoids are hampering these clinical applications. Therefore, there is a clear need for clinically relevant alternative culture substrates which can unlock the full potential of the hepatobiliary organoids for future TERM applications. Synthetic hydrogel alternatives are interesting substitutes. They can be tuned and chemically modified with relative ease. However, they are often too simplistic when it comes to mimicking the biochemical complexity of the LECM [28,30]. 'Fine--tuning' of their composition with natural ECM components and/or synthetic ECM substitute until they can fully substitute the LECM is challenging [25]. On the other hand, the use of ECM extracts from healthy decellularized livers circumvent the need for 'fine-tuning' and is, therefore, an attractive method for creating dynamic tissue-specific and bioactive microenvironments *in vitro* [30,54–56].

In theory, ECM components should be highly preserved between species [11,57], and therefore, extracts from human and porcine livers are both of interest. However, we observed differences between PLECM and HLECM, as PLECM could be fully digested, whereas HLECM contained undigested ECM particles. This is likely due to accumulation of age-related damage and/or non-enzymatic cross-linking of ECM molecules in aged human livers (average age human livers: 56 years, SD:±24 years) [58]. This in turn can prohibit the pepsin enzyme from digestion of the ECM [59,60]. In fact, these biological differences are one of the disadvantages of using tissue-derived products as these differences create batch-to-batch differences. This has also been described for BME, where batch variance up-to 50% have been measured [12]. However, 100 g of lyophilized HLECM could, for example, yield ±5,000 ml of HLECM extracts at a protein concentration of 6 mg/ml (Stock concentration). Therefore, single human-sized livers should yield plenty of LECM extracts for large experiments using the same batch of LECM. Moreover, multiple livers can be pooled together to mitigate biological variances.

Porcine livers can be obtained easily from bio-industry. Moreover, they can be obtained from animals in the same (young) age-range, which could minimize the effect of the aforementioned accumulated damage and crosslinking of the ECM during the life span. However, the transmission of zoonotic diseases, such as the PERV, is a risk associated with the use of porcine tissue [44,61–63]. The PERV-pol gene was not detectable after decellularization by conventional PCR techniques, thereby potentially reducing the risk of transmission. Similar (clinical) research using porcine-derived ECM products, such as heart valves, have not found any evidence of transmission [62,63]. PLECM could therefore be an interesting alternative source of livers for creating tissue-specific culture substrates for ICO. Animals could in the future be bred in controlled environments to further mitigate the risk of disease transmission. Moreover, multiple tissues for other tissue engineering applications could be harvested from the same animal.

LECM extracts have shown to be able to maintain hepatic phenotypes of hepatocytes [54–56], liver sinusoidal endothelial cells and hepatic stellate cells *in vitro* [64]. Moreover, LECM supported formation of complex biliary networks by cholangiocyte cell-lines [65] and improved differentiation capacity of stem cells [51–53,66]. Based upon this research, it was expected that switching from the laminin-rich BME to collagen-based tissue specific LECM extracts could improve the differentiation of ICO towards hepatocyte-like cells. However, we could not show improvement in differentiation in our study. In fact, the use of LECM also did not significantly alter the expression of selected hepatobiliary proteins and genes in expansion medium. Moreover, it did not alter the cell viability of the ICO. The most pronounced difference between ICO grown in BME or LECM was the lower proliferation rates for the ICO grown in LECM. These results could indicate that the phenotype of the ICO is more dictated by the culture medium and its components than by the ECM components.

Cell-matrix interactions were observed for ICO grown in LECM extracts, as the LECM domes in which ICO were grown often showed (partial) contraction of dome. Similar findings have been reported for other cell and ECM-derived hydrogels [67,68]. The LECM hydrogels were relatively weak and cells could condense them. By doing so, the ICO could have 'normalized' their local environment, thereby mitigating the effect of different LECM concentrations. However, studying the effect of different (bio) physical characteristics is of interest, as these mechano-modulatory signals play important roles in cell survival, proliferation and differentiation [19,24–27,69]. The mechanical rigidity of LECM can be improved by chemical modification by adding different 'polymer backbones' and/or cross-linkers. By doing so, the mechanical properties can be altered without altering the biochemical concentration of LECM [24,25,70]. Of note, LECM extracts can also be used to 'enrich' other (synthetic) hydrogels in an effort to create more tissue-specific hydrogels and/or bio-inks for three-dimensional printing [70]. This way the LECM extracts can also be utilized to reconstruct tissue-specific micro-environments for hepatobiliary disease modelling [22].

Hepatocyte functionality tests are the most important proof of

successful hepatocyte differentiation. However, since the differentiation was not improved over previously published protocols [1,10], hepatocyte functionality was not assessed. Nevertheless, the ability to obtain both functional cholangiocytes and hepatocytes from the same ICO, would be valuable for TERM applications [71]. Perhaps, differentiation to hepatocytes can be improved with more complex and extended differentiation protocols, which include growth factor gradients.

For TERM applications, vast amounts of cells are required. Currently used culture methods (in small 25 μl hydrogel domes) is laborious and time-consuming. Schneeberger et al. showed that dynamic cultures in spinner flasks allow for large scale expansion of ICO [5]. Our results with spinner flasks show feasibility of culturing ICO using HLECM under dynamic conditions. However, the relative increase of cells in HLECM was lower compared to the numbers for BME reported by Schneeberger et al. Although the cell yield was not comparable, culturing ICO under dynamic conditions was less time consuming and more efficient when compared to normal static culture in domes. Moreover, the spinner flaks could in the future allow for automation of certain steps of the culture process (e.g. medium refreshment). Automation reduces the risk of human error in production of clinically relevant cells. To prevent the formation of large cell aggregates in future application, increased viscosity by changing HLECM concentration or addition of inert viscous agents could potentially create more homogenized cultures and further improve proliferation capacity.

ICO are not the only cholangiocyte organoids which could benefit from clinically relevant culture substrates. In recent years, different patient-derived cholangiocyte organoid cultures have also been established from extrahepatic bile duct (extrahepatic cholangiocyte organoids: ECO) [72,73] and bile samples (Bile derived cholangiocyte organoids: BCO) [74,75]. These organoids retain cholangiocyte-specific characteristics [76,77] and can be used for various biliary TERM applications, such repopulation of decellularized EBD scaffolds [78], reconstruction of bile duct *in vitro* [73,79] and bile duct repair after (ischemic) damage [7].

Mouse tumor-derived BME hamper the clinical application of patient-derived cholangiocyte organoids for TERM applications. ECM extracts derived from healthy decellularized human or porcine liver are clinically relevant replacements. These LECM extracts can replace BME as a culture substrate for ICO expansion. Subtle differences, such as lower proliferation rates, were noted, but ICO do not change expression of cholangiocyte-specific markers upon switching to LECM extracts. Moreover, LECM extracts allowed for the successful initiation and large-scale expansion of the organoids, providing a basis for complete BME-free culture methods.

Author contributions

JW, JDJ, LJWL and MMAV designed the study. MMAV, JDJ and LJWL obtained funding. IJS procured and collected livers. IJS and JW performed decellularization of livers. DV and JW performed pepsin digestion experiments and subsequent analysis. HPR isolated RNA and DNA and performed PERV analysis. BCJE performed nanoindentation experiments. YYK and PER collected liver biopsies and initiated ICO in BME. YYK, EVAH, DLV, GST cultured ICO in LECM. GST performed culturing for SILAC experiments. OR and GWT performed MS analysis and together with GST performed the analysis of the SILAC data. YYK and JW performed differentiation experiments. EVAH, BS, KS and JW performed spinner flask experiments. JW and GST collected all data, performed analysis and drafted the figures. JW, GST, BS, LJWL, JDJ and MMAV wrote the manuscript.

Declaration of competing interest

The authors declare that they have no known competing financial interests or personal relationships that could have appeared to influence the work reported in this paper.

Acknowledgements

We would like to thank Dr. Bram Zoetebier from the University of Twente for assistance on performing shear rheology experiment. This project was funded by a 'Medical Delta Regenerative Medicine 4D: Generating complex tissues with stem cells and printing technology' grant, a TKI-LSH grant (EMC-LSH19002) and a Gastrostart grant from the Dutch Society for GastroEnterology (NVGE).

Appendix A. Supplementary data

Supplementary data to this article can be found online at https://doi.org/10.1016/j.biomaterials.2022.121473.

References

[1] M. Huch, H. Gehart, et al., Long-term culture of genome-stable bipotent stem cells from adult human liver, Cell 160 (1–2) (2015) 299–312.
[2] R. Lanza, R. Langer, et al., Principles of Tissue Engineering, Academic press, 2020.
[3] J.P. Vacanti, R. Langer, Tissue engineering: the design and fabrication of living replacement devices for surgical reconstruction and transplantation, Lancet 354 (1999) S32–S34.
[4] G. Mazza, W. Al-Akkad, et al., Liver tissue engineering: from implantable tissue to whole organ engineering, Hepatol. Commun. 2 (2) (2018) 131–141.
[5] K. Schneeberger, N. Sánchez-Romero, et al., Large-scale production of LGR5-positive bipotential human liver stem cells, Hepatology (2020) 257–270.
[6] J. Willemse, R. Lieshout, et al., From organoids to organs: bioengineering liver grafts from hepatic stem cells and matrix, Best Pract. Res. Clin. Gastroenterol. 31 (2) (2017) 151–159.
[7] F. Sampaziotis, D. Muraro, et al., Cholangiocyte organoids can repair bile ducts after transplantation in the human liver, Science 371 (6531) (2021) 839–846.
[8] D. Eshmuminov, D. Becker, et al., An integrated perfusion machine preserves injured human livers for 1 week, Nat. Biotechnol. 38 (2) (2020) 189–198.
[9] J. Willemse, M.M.A. Verstegen, et al., Fast, robust and effective decellularization of whole human livers using mild detergents and pressure controlled perfusion, Mater. Sci. Eng. C 108 (2020) 110200.
[10] M.M.A. Verstegen, F.J.M. Roos, et al., Human extrahepatic and intrahepatic cholangiocyte organoids show region-specific differentiation potential and model cystic fibrosis-related bile duct disease, Sci. Rep. 10 (1) (2020) 21900.
[11] S.F. Badylak, D. Taylor, et al., Whole-organ tissue engineering: decellularization and recellularization of three-dimensional matrix scaffolds, Annu. Rev. Biomed. Eng. 13 (2011) 27–53.
[12] C.S. Hughes, L.M. Postovit, et al., Matrigel: a complex protein mixture required for optimal growth of cell culture, Proteomics 10 (9) (2010) 1886–1890.
[13] H.K. Kleinman, G.R. Martin, Matrigel: basement membrane matrix with biological activity, Semin. Cancer Biol. 15 (5) (2005) 378–386.
[14] G. Benton, I. Arnaoutova, et al., Matrigel: from discovery and ECM mimicry to assays and models for cancer research, Adv. Drug Deliv. Rev. 79–80 (2014) 3–18.
[15] H.K. Kleinman, Preparation of basement membrane components from EHS tumors, Curr. Protocols Cell Biol. (1998), 00(1): p. 10.2.1-10.2.10.
[16] S. Vukicevic, H.K. Kleinman, et al., Identification of multiple active growth factors in basement membrane Matrigel suggests caution in interpretation of cellular activity related to extracellular matrix components, Exp. Cell Res. 202 (1) (1992) 1–8.
[17] C. Xu, M.S. Inokuma, et al., Feeder-free growth of undifferentiated human embryonic stem cells, Nat. Biotechnol. 19 (10) (2001) 971–974.
[18] L. Hagbard, K. Cameron, et al., Developing defined substrates for stem cell culture and differentiation, Philos. Trans. R. Soc. Lond. Ser. B Biol. Sci. 373 (1750) (2018) 20170230.
[19] M. Klaas, T. Kangur, et al., The alterations in the extracellular matrix composition guide the repair of damaged liver tissue, Sci. Rep. 6 (1) (2016) 27398.
[20] A. Baiocchini, C. Montaldo, et al., Extracellular matrix molecular remodeling in human liver fibrosis evolution, PLoS One 11 (3) (2016) e0151736.
[21] R.C. Benyon, M.J. Arthur, Extracellular matrix degradation and the role of hepatic stellate cells, Semin. Liver Dis. 21 (3) (2001) 373–384.
[22] G. van Tienderen, G. Koerkamp, et al., Recreating tumour complexity in a dish: organoid models to study liver cancer cells and their extracellular environment, Cancers 11 (2019) 1706.
[23] R.O. Hynes, The extracellular matrix: not just pretty fibrils, Science (New York, N Y) 326 (5957) (2009) 1216–1219.
[24] G. Sorrentino, S. Rezakhani, et al., Mechano-modulatory synthetic niches for liver organoid derivation, Nat. Commun. 11 (1) (2020) 3416.
[25] N. Gjorevski, N. Sachs, et al., Designer matrices for intestinal stem cell and organoid culture, Nature 539 (7630) (2016) 560–564.
[26] M. Krüger, L.A. Oosterhoff, et al., Cellulose nanofibril hydrogel promotes hepatic differentiation of human liver organoids, Adv. Healthc. Mater. 9 (6) (2020) 1901658.
[27] S. Ye, J.W.B. Boeter, et al., A chemically defined hydrogel for human liver organoid culture, Adv. Funct. Mater. 30 (48) (2020) 2000893.
[28] S. Ye, J.W.B. Boeter, et al., Hydrogels for liver tissue engineering, Bioengineering (Basel, Switzerland) 6 (3) (2019) 59.

[29] M. Krüger, L.A. Oosterhoff, et al., Cellulose nanofibril hydrogel promotes hepatic differentiation of human liver organoids, Adv. Healthc. Mater. 9 (6) (2020) e1901658.
[30] L.T. Saldin, M.C. Cramer, et al., Extracellular matrix hydrogels from decellularized tissues: structure and function, Acta Biomater 49 (2017) 1–15.
[31] C. Gazia, R. Tamburrini, et al., Extracellular matrix-based hydrogels obtained from human tissues: a work still in progress, Curr. Opin. Organ Transplant. 24 (5) (2019) 604–612.
[32] G.S. Hussey, J.L. Dziki, et al., Extracellular matrix-based materials for regenerative medicine, Nat. Rev. Mater. 3 (7) (2018) 159–173.
[33] M. Parmaksiz, A. Dogan, et al., Clinical applications of decellularized extracellular matrices for tissue engineering and regenerative medicine, Biomed. Mater. 11 (2) (2016) 22003.
[34] M.T. Kozlowski, C.J. Crook, et al., *Towards organoid culture without Matrigel.* Communications Biology 4 (1) (2021) 1387.
[35] S. Tas, D.A. Bölükbas, et al., Decellularized extracellular matrix hydrogels for human airway organoid culture, ERJ Open Res. 7 (suppl 6) (2021) 101.
[36] S. Kim, Y.S. Choi, et al., Intestinal extracellular matrix hydrogels to generate intestinal organoids for translational applications, J. Ind. Eng. Chem. (2021) 155–164.
[37] R. Simsa, T. Rothenbücher, et al., Brain organoid formation on decellularized porcine brain ECM hydrogels, PLoS One 16 (1) (2021) e0245685.
[38] M. Vermeulen, F. Del Vento, et al., Generation of organized porcine testicular organoids in solubilized hydrogels from decellularized extracellular matrix, Int. J. Mol. Sci. 20 (21) (2019) 5476.
[39] E. Lada, M. Anna, et al., Porcine liver anatomy applied to biomedicine, J. Surg. Res. 250 (2020) 70–79.
[40] A. Acun, R. Oganesyan, et al., Liver donor age affects hepatocyte function through age-dependent changes in decellularized liver matrix, Biomaterials 270 (2021) 120689.
[41] S. Becker, M. Saint-Cyr, et al., AlloDerm versus DermaMatrix in immediate expander-based breast reconstruction: a preliminary comparison of complication profiles and material compliance, Plast. Reconstr. Surg. 123 (1) (2009) 1–6, discussion 107-8.
[42] S. Brooke, J. Mesa, et al., Complications in tissue expander breast reconstruction: a comparison of AlloDerm, DermaMatrix, and FlexHD acellular inferior pole dermal slings, Ann. Plast. Surg. 69 (4) (2012) 347–349.
[43] T.W. Gilbert, J.M. Freund, et al., Quantification of DNA in biologic scaffold materials, J. Surg. Res. 152 (1) (2009) 135–139.
[44] L. Krüger, Y. Kristiansen, et al., A comprehensive strategy for screening for xenotransplantation-relevant viruses in a second isolated population of Göttingen minipigs, Viruses 12 (1) (2019).
[45] L. Broutier, A. Andersson-Rolf, et al., Culture and establishment of self-renewing human and mouse adult liver and pancreas 3D organoids and their genetic manipulation, Nat. Protoc. 11 (9) (2016) 1724–1743.
[46] L.J. Van Der Laan, Christopher Lockey, Bradley C. Griffeth, Francine S. Frasier, Carolyn A. Wilson, David E. Onions, Bernhard J. Hering, Infection by porcine endogenous retrovirus after islet xenotransplantation in SCID mice, Nature 407 (2000) 90–94.
[47] M. Meyer, Processing of collagen based biomaterials and the resulting materials properties, Biomed. Eng. Online 18 (1) (2019) 24.
[48] J.-M. Banales, J. Prieto, et al., Cholangiocyte anion exchange and biliary bicarbonate excretion, World J. Gastroenterol. 12 (22) (2006) 3496–3511.
[49] K.O. West, H.M. Scott, et al., The Splicing Factor hnRNP M Is a Critical Regulator of Innate Immune Gene Expression in Macrophages, 2019, p. 617043, bioRxiv.
[50] A. Emadali, B. Muscatelli-Groux, et al., Proteomic analysis of ischemia-reperfusion injury upon human liver transplantation reveals the protective role of IQGAP1* S, Mol. Cell. Proteomics 5 (7) (2006) 1300–1313.
[51] M. Jaramillo, H. Yeh, et al., Decellularized human liver extracellular matrix (hDLM)-mediated hepatic differentiation of human induced pluripotent stem cells (hIPSCs), J. Tissue Eng. Regen. Med. 12 (4) (2018) e1962–e1973.
[52] D. Vyas, P.M. Baptista, et al., Self-assembled liver organoids recapitulate hepatobiliary organogenesis in vitro, Hepatology 67 (2) (2018) 750–761.
[53] B. Wang, A.E. Jakus, et al., Functional maturation of induced pluripotent stem cell hepatocytes in extracellular matrix—a comparative analysis of bioartificial liver microenvironments, STEM CELLS Transl. Med. 5 (9) (2016) 1257–1267.
[54] A.E. Loneker, D.M. Faulk, et al., Solubilized liver extracellular matrix maintains primary rat hepatocyte phenotype in-vitro, J. Biomed. Mater. Res. 104 (4) (2016) 957–965.
[55] J.S. Lee, J. Shin, et al., Liver extracellular matrix providing dual functions of two-dimensional substrate coating and three-dimensional injectable hydrogel platform for liver tissue engineering, Biomacromolecules 15 (1) (2014) 206–218.
[56] R. Grant, J. Hallett, et al., Blended electrospinning with human liver extracellular matrix for engineering new hepatic microenvironments, Sci. Rep. 9 (1) (2019) 6293.
[57] T.W. Gilbert, Strategies for tissue and organ decellularization, J. Cell. Biochem. 113 (7) (2012) 2217–2222.
[58] J.G. Snedeker, A. Gautieri, The role of collagen crosslinks in ageing and diabetes - the good, the bad, and the ugly, Muscles Ligaments Tendons J. 4 (3) (2014) 303–308.
[59] P.L. Lewis, J. Su, et al., Complex bile duct network formation within liver decellularized extracellular matrix hydrogels, Sci. Rep. 8 (1) (2018) 1–14.
[60] C. Williams, K. Sullivan, et al., Partially digested adult cardiac extracellular matrix promotes cardiomyocyte proliferation in vitro, Adv. Healthc. Mater. 4 (10) (2015) 1545–1554.
[61] A.W. Godehardt, R. Ramm, et al., Decellularized pig pulmonary heart valves—depletion of nucleic acids measured by proviral PERV pol, Xenotransplantation 27 (2) (2020) e12565.
[62] K. Łopata, E. Wojdas, et al., Porcine endogenous retrovirus (PERV) - molecular structure and replication strategy in the context of retroviral infection risk of human cells, Front. Microbiol. 9 (2018), p. 730-730.
[63] K. Kallenbach, R.G. Leyh, et al., Guided tissue regeneration: porcine matrix does not transmit PERV, Biomaterials 25 (17) (2004) 3613–3620.
[64] N. Alevra Sarika, V.L. Payen, et al., Human liver-derived extracellular matrix for the culture of distinct human primary liver cells, Cells 9 (6) (2020) 1357.
[65] P.L. Lewis, J. Su, et al., Complex bile duct network formation within liver decellularized extracellular matrix hydrogels, Sci. Rep. 8 (1) (2018) 12220.
[66] M. Saheli, M. Sepantafar, et al., Three-dimensional liver-derived extracellular matrix hydrogel promotes liver organoids function, J. Cell. Biochem. 119 (6) (2018) 4320–4333.
[67] M.T. Wolf, K.A. Daly, et al., A hydrogel derived from decellularized dermal extracellular matrix, Biomaterials 33 (29) (2012) 7028–7038.
[68] J. Fernández-Pérez, M. Ahearne, The impact of decellularization methods on extracellular matrix derived hydrogels, Sci. Rep. 9 (1) (2019) 14933.
[69] S.S. Desai, J.C. Tung, et al., Physiological ranges of matrix rigidity modulate primary mouse hepatocyte function in part through hepatocyte nuclear factor 4 alpha, Hepatology 64 (1) (2016) 261–275.
[70] A. Skardal, M. Devarasetty, et al., A hydrogel bioink toolkit for mimicking native tissue biochemical and mechanical properties in bioprinted tissue constructs, Acta Biomater 25 (2015) 24–34.
[71] M.M.A. Verstegen, J. Willemse, et al., Decellularization of whole human liver grafts using controlled perfusion for transplantable organ bioscaffolds, Stem Cell. Dev. 26 (18) (2017) 1304–1315.
[72] M. Verstegen, F. Roos, et al., Human extrahepatic and intrahepatic cholangiocyte organoids show region-specific differentiation potential and model cystic fibrosis-related bile duct disease, Sci. Rep. 10 (2020).
[73] F. Sampaziotis, A.W. Justin, et al., Reconstruction of the mouse extrahepatic biliary tree using primary human extrahepatic cholangiocyte organoids, Nat. Med. 23 (8) (2017) 954–963.
[74] C.J. Soroka, D.N. Assis, et al., Bile-derived organoids from patients with primary sclerosing cholangitis recapitulate their inflammatory immune profile, Hepatology 70 (3) (2019) 871–882.
[75] F.J.M. Roos, H. Wu, et al., Cholangiocyte organoids from human bile retain a local phenotype and can repopulate bile ducts in vitro, Clin. Transl. Med. 11 (12) (2021) e566.
[76] L. Aloia, M.A. McKie, et al., Epigenetic remodelling licences adult cholangiocytes for organoid formation and liver regeneration, Nat. Cell Biol. 21 (11) (2019) 1321–1333.
[77] C.A. Rimland, S.G. Tilson, et al., Regional differences in human biliary tissues and corresponding in vitro derived organoids, Hepatology (2020) 247–267.
[78] J. Willemse, F.J.M. Roos, et al., Scaffolds obtained from decellularized human extrahepatic bile ducts support organoids to establish functional biliary tissue in a dish, Biotechnol. Bioeng. 118 (2) (2021) 836–851.
[79] C. Chen, P.G.M. Jochems, et al., Bioengineered bile ducts recapitulate key cholangiocyte functions, Biofabrication 10 (3) (2018) 34103.